

# **A lipocalin mediates unidirectional haem biomineralization in malaria parasites**

Joachim M. Matz<sup>1,2,\*</sup>, Benjamin Drepper<sup>2</sup>, Thorsten B. Blum<sup>3</sup>, Eric van Genderen<sup>3</sup>,  
Alana Burrell<sup>4</sup>, Peer Martin<sup>2</sup>, Thomas Stach<sup>2</sup>, Lucy Collinson<sup>4</sup>, Jan Pieter  
Abrahams<sup>3,5,6</sup>, Kai Matuschewski<sup>2</sup> & Michael J. Blackman<sup>1,7</sup>

<sup>1</sup> Malaria Biochemistry Laboratory, The Francis Crick Institute, London, UK

<sup>2</sup> Department of Molecular Parasitology, Institute of Biology, Humboldt University, Berlin, Germany

<sup>3</sup> Laboratory of Nanoscale Biology, Division of Biology and Chemistry, Paul Scherrer Institute, Villigen, Switzerland

<sup>4</sup> Electron Microscopy Science Technology Platform, The Francis Crick Institute, London, UK

<sup>5</sup> Center for Cellular Imaging and NanoAnalytics, Biozentrum, University of Basel, Basel, Switzerland.

<sup>6</sup> Institute of Biology, Leiden University, Leiden, The Netherlands.

<sup>7</sup> Faculty of Infectious and Tropical Diseases, London School of Hygiene & Tropical Medicine, London, UK

\* Corresponding author: J.M.M., [joachim.matz@crick.ac.uk](mailto:joachim.matz@crick.ac.uk), <https://orcid.org/0000-0002-0575-0412>

## ABSTRACT

During blood stage development, malaria parasites are challenged with the detoxification of enormous amounts of haem released during the proteolytic catabolism of erythrocytic haemoglobin. They tackle this problem by sequestering haem into bioinert crystals known as haemozoin. The mechanisms underlying this biomineralization process remain enigmatic. Here, we demonstrate that both rodent and human malaria parasite species secrete and internalize a lipocalin-like protein, PV5, to control haem crystallization. Transcriptional deregulation of *PV5* in the rodent parasite *Plasmodium berghei* results in inordinate elongation of haemozoin crystals, while conditional *PV5* inactivation in the human malaria agent *Plasmodium falciparum* causes excessive multi-dimensional crystal branching. Electron diffraction analysis indicates that neither the crystalline order nor unit cell of haemozoin are affected by impaired *PV5* function. Deregulation of *PV5* expression renders *P. berghei* hypersensitive to the antimalarial drugs artesunate, chloroquine, and atovaquone, resulting in accelerated parasite clearance following drug treatment *in vivo*. Together, our findings demonstrate the *Plasmodium*-tailored role of a lipocalin family member in haemozoin formation and underscore the haem biomineralization pathway as an attractive target for therapeutic exploitation.

## KEYWORDS

*Plasmodium*, malaria, haemozoin, vacuole, lipocalin

## SIGNIFICANCE

During blood stage development, the malaria parasite replicates inside erythrocytes of the vertebrate host, where it engulfs and digests most of the available haemoglobin. This results in release of the oxygen-binding prosthetic group haem, which is highly toxic in its unbound form. The parasite crystallizes the haem into an insoluble pigment called haemozoin, a process that is vital for parasite survival and which is exploited in antimalarial therapy. We demonstrate that the parasite uses a protein called *PV5* in haemozoin formation and that interfering with *PV5* expression increases the parasite's sensitivity to antimalarial drugs during blood infection. An improved understanding of the mechanism underlying haem sequestration will provide valuable insights for future drug development efforts.

## INTRODUCTION

The devastating pathology of malaria is caused by infection of red blood cells with unicellular *Plasmodium* parasites which reside within an intraerythrocytic parasitophorous vacuole (PV) (1). Throughout blood stage development, the parasite ingests up to 80% of the host cell cytoplasm, facilitating amino acid acquisition and making sufficient room for parasite growth (2, 3). Haemoglobin breakdown is carried out by an array of functionally redundant proteases and occurs in acidified lysosome-like organelles with species-specific morphology (4). In the rodent-infective parasite species *Plasmodium berghei*, one or more haemoglobin-containing food vacuoles (FV) give rise to small digestive vesicles (DVs) where active haemoglobin catabolism occurs and which only fuse at the very end of intraerythrocytic development (5). By contrast, the most virulent agent of human malaria, *Plasmodium falciparum*, directs all endosomal traffic to a single large FV, where proteolysis occurs. The DVs of *P. berghei* and the FV of *P. falciparum* are therefore functionally equivalent (6).

Here, haemoglobin digestion is accompanied by the release from the globin chains of high levels of the porphyrin co-factor haem, which can damage proteins and lipids through various mechanisms, including the formation of free radicals (7). The unique challenge of haem detoxification is met by the parasite's capacity to sequester the released haem into a bioinert crystalline product called haemozoin (Hz), which accumulates in the FV or DVs. Haem is initially oxidised to yield haematin, which then dimerizes through the reciprocal coordination of iron and propionate moieties. This molecular unit then assembles into crystals which typically take the form of triclinic high aspect ratio parallelograms (8-10). By the end of intraerythrocytic development, all the Hz crystals are contained within a central residual body, which is eventually released upon parasite egress from the host cell and which contributes to the inflammatory responses associated with acute malaria (11). The mechanism of Hz formation is highly debated. While several studies suggest a conventional physicochemical and autocatalytic crystallization mechanism (12-15), there have been reports of parasite proteins (16-18) and lipids (19-21) promoting Hz assembly *in vitro*.

The parasite's dependency on haem detoxification has long been exploited in antimalarial therapy with outstanding success. Aminoquinolines inhibit Hz formation *via* direct physical interactions with haematin and the crystal surface, eventually leading to the build-up of cytotoxic free haem (22-25). The aminoquinoline chloroquine was the front-line medication against malaria from the 1950s onward until the emergence of wide-spread drug resistance restricted its utility (26). Nonetheless, to this day, chloroquine remains among the most effective antimalarial drugs ever developed, highlighting the outstanding importance of haem

81 sequestration for *Plasmodium* survival. It is thus crucial for future drug development efforts to  
82 gain a better understanding of the mechanisms underlying this unique biomineralization event.

83 In this report, we demonstrate that a parasite lipocalin-like protein called PV5 is a  
84 central regulator of *H*<sub>2</sub> formation.

## RESULTS

### Malaria parasites encode a lipocalin-like protein, PV5

Employing a genome-wide *in silico* down-scaling approach, we previously identified an essential *P. berghei* PV protein, *PbPV5*, which has orthologues in all other *Plasmodium* species (27). Inspection of the PV5 amino acid sequence revealed a striking similarity to members of the functionally diverse lipocalin family, barrel-shaped proteins capable of binding various hydrophobic ligands and/or protein interaction partners (28). The signature lipocalin fold comprises a short amino-terminal helix followed by eight consecutive barrel-forming  $\beta$ -strands, another  $\alpha$ -helix and one more  $\beta$ -strand (Fig. 1A) (29). In addition, PV5 harbours two preceding amino-terminal  $\beta$ -strands specific to *Plasmodium*, as well as a signal peptide. Multiple sequence alignments with lipocalins from phylogenetically distant organisms showed the presence of a highly conserved glycine and two aromatic amino acids within the structurally conserved region 1 (SCR1) of PV5, a hallmark of the extended calycin superfamily (Fig. 1A) (29). Among several structural homologues, the bacterial outer membrane lipocalin Blc from *Escherichia coli* was predicted to share the highest similarity with PV5. Blc-guided structure homology modelling suggests that PV5 shares the overall architecture of the lipocalin family including the characteristic  $\beta$ -barrel (Fig. 1B). Together, the sequence signatures and predicted structural features support membership of *Plasmodium* PV5 in the calycin protein superfamily.

### PV5 localizes to the PV and DVs in *P. berghei*

We first investigated the spatiotemporal expression of *PbPV5* during asexual blood stage development. Live fluorescence microscopy of transgenic *P. berghei* parasites expressing mCherry-3xMyc-tagged *PbPV5* confirmed that *PbPV5* localizes to tubular PV extensions during ring and trophozoite stages and surrounds individual merozoites in segmented schizonts (Fig. 1C) (27). In addition, a substantial fraction of the protein was restricted to the parasite cytoplasm. This was particularly prominent in schizonts, where intraparasitic *PbPV5* appeared to localize to the Hz-containing residual body (Fig. 1C). In merozoites, mCherry fluorescence was concentrated in a punctate intraparasitic region, perhaps signifying storage of *PbPV5* in the dense granules, as has been demonstrated for several other important PV proteins (30-32), but this fraction was minimal as compared to the protein contained in the residual body. Quantification of the mCherry-fluorescence intensity in live parasites indicated that *PbPV5* is much more abundant in mature parasite stages than in rings and merozoites, suggesting substantial levels of *de novo* synthesis throughout parasite maturation (Fig 1C).

In trophozoites, the intraparasitic fraction of *PbPV5* was associated with spherical structures at the parasite periphery (Fig. 1C) and microscopic examination of mechanically expanded free parasites revealed that these were the Hz-containing DVs (Fig. 1D). Here, *PbPV5* was freely soluble, as indicated by subcellular parasite fractionation (Fig. 1E). Together, our observations suggest that *PbPV5* is a calycin family member that is first secreted into the PV and then internalized during endocytosis of host cell cytoplasm to accumulate in the matrix of the DVs.

## **Transcriptional deregulation of *PbPV5* impairs asexual parasite propagation *in vivo***

Our previous attempts to disrupt the genomic *PbPV5* locus resulted only in atypical integration of the targeting construct without perturbing the endogenous gene, which is indicative of essential functions during the asexual blood stage cycle *in vivo* (27). As an alternative genetic strategy to analyse *PbPV5* function, we sought to deregulate *PbPV5* expression by employing a promoter swap approach (Fig. 2A). We thus generated parasites expressing the endogenous *PbPV5* gene from the promoters of *Plasmodium* translocon of exported proteins 88 (*PTEX88*) or heat shock protein 101 (*HSP101*), respectively (*SI Appendix*, Fig. S1 A and B). Previously published RNA sequencing data predicted that expression under these heterologous promoters would result in considerable downregulation to 2–20% of WT *PbPV5* steady state transcript levels, respectively, depending on the developmental stage (33). However, quantitative real-time PCR analysis of the mutants indicated that the knock-down efficiency was only ~60% in asynchronous blood stages (*SI Appendix*, Fig. S1C). These differences did not reach statistical significance, likely due to variation in the composition of the mixed blood stages. By contrast, mutant schizonts exhibited significantly elevated *PbPV5* transcript levels, corresponding to ~3.4 (*pv5::5'ptex88*) and ~5.6 times (*pv5::5'hsp101*) more than in WT schizonts (*SI Appendix*, Fig. S1C). These unexpected dynamics might be explained by compensatory mechanisms and/or locus-dependent promoter activities. Importantly, using the promoter swap strategy, we succeeded in deregulating the physiological expression of *PbPV5*.

To investigate whether altered *PbPV5* transcription results in reduced parasite fitness, we examined asexual propagation of the mutants *in vivo*. Growth of the promoter swap mutants was significantly impaired, with the *pv5::5'ptex88* parasites growing at 80% and *pv5::5'hsp101* parasites at only 54% of the WT growth rate (Fig. 2B). These results underline the importance of correct *PbPV5* expression during asexual replication of the parasite *in vivo* (Fig. 2B).

## **PbPV5 mutants form less Hz**

Inspection of Giemsa-stained thin blood films revealed striking morphological differences between WT parasites and the promoter swap mutants. During the trophozoite stage, the FV of the mutants was significantly swollen, visible as a translucent area within the parasite cytoplasm close to the nucleus (Fig. 2C). Microscopic quantification revealed this area to be 1.5-fold (*pv5::5'ptex88*) or 1.8-fold (*pv5::5'hsp101*) larger than in WT parasites (*SI Appendix*, Fig. S2A). Vacuolar swelling was transient, as mature schizonts did not exhibit comparable abnormalities (Fig. 2C).

Another striking phenomenon was the low visibility of dark granular material in mutant trophozoites, when compared to WT (Fig. 2C). This was most noticeable in the *pv5::5'hsp101* mutant and became particularly apparent during the gametocyte stage, where pigment granules are usually very prominent. To validate the visually observed lack of granularity, we subjected mixed blood stage parasites to flow cytometry and measured the intensity of the side scattered light, a commonly used proxy for cellular granularity (*SI Appendix*, Fig. S2B). In agreement with our microscopic analysis, the PbPV5 mutants displayed reduced side scattering and the phenotype was again more severe in the *pv5::5'hsp101* mutant.

Because we suspected a Hz formation defect in the mutants, we fixed intraerythrocytic parasites with methanol and subjected them to reflection contrast polarized light microscopy, which exploits the birefringent properties of Hz to specifically visualize the crystals. Using this method, we detected a weaker signal for the mutants, which correlated with reduced visibility of dark pigment in brightfield (Fig. 2D). Enumeration of individual bright entities suggested the presence of fewer Hz-containing structures within the mutants (~80% of WT) (Fig. 2D). Quantification of the reflected polarized light intensity also indicated that *pv5::5'ptex88* parasites form only 64% and the *pv5::5'hsp101* 61% of the Hz generated in WT parasites (*SI Appendix*, Fig. S2C). Together, these observations show that perturbation of PbPV5 expression results in reduced haem biomineralization *in vivo*.

## **Protracted Hz extension upon deregulation of PbPV5 expression**

We next aimed to examine how lower levels of Hz correlate with crystal size. To do this we isolated Hz from mixed blood stage parasites and examined the material by scanning electron microscopy (SEM). This confirmed the characteristic high aspect ratio parallelogram morphology of WT Hz (Fig. 2 E and F). Strikingly, this was not the case for crystals isolated from the promoter swap mutants. Hz from both transgenic parasite strains exhibited highly irregular shapes and rough edges and showed only few of the distinctive Hz crystal vertices (Fig. 2F). Crystals from *pv5::5'ptex88* parasites most often had a pointed and canine tooth-

like appearance, extending from a single straight crystal face. These abnormalities were even more pronounced in the *pv5::5'hsp101* mutant, where in most cases there was a region of normal crystal morphology with 2 or 3 straight edges, corresponding to the {010}, {011} and {001} faces. From this regular parent crystal emerged an enormous outgrowth which usually surpassed the dimensions of the parent crystal (Fig. 2F). This outgrowth consistently grew at an obtuse angle of  $\sim 105^\circ$  in relation to the dominant *c* axis of the parent crystal, although accurate determination of the angle was complicated by the slightly bent and irregular shape of the outgrowth, which might be attributed to the space restrictions encountered in the *P. berghei* DVs. The outgrowth's angle was not reflected in the physiological morphology of Hz (Fig. 2E and F) and at least two faces of the regular parent crystal appeared to be involved. Indeed, in most cases, the outgrowth emerged from sites where the {010} and {011} faces meet and always grew along a plane corresponding to one of the original crystal faces (Fig. 2F). Other crystal formations were also observed, albeit at lower frequency, including some with multiple crystal branches and some with very rough surfaces (*SI Appendix*, Fig. S2D). We observed similar crystal abnormalities *in situ* by transmission electron microscopy (TEM) of purified schizonts (Fig. 2G).

Despite the lower overall levels of Hz formed and the abnormal crystal morphology, we found that the mutants formed larger Hz crystals as indicated by the area exposed to the SEM electron beam (Fig. 2H). The *pv5::5'hsp101* mutant formed the largest crystals, which were  $\sim 177\%$  of WT size, while the *pv5::5'ptex88* crystals were at 130%. Importantly, the mutant Hz crystals displayed greater dimensions only in length but not in width owing to the unidirectional expansion of the outgrowth (Fig. 2H). Examination of the parent crystals from *pv5::5'hsp101* parasites showed that these were roughly half the size of whole WT crystals (Fig. 2H). The aspect ratios of WT crystals and the *pv5::5'hsp101* parent crystals were identical, together indicating that a period of normal crystallisation during earlier *pv5::5'hsp101* parasite development is followed by irregular crystal extension later on (*SI Appendix*, Fig. S2E). Inspection of Hz from an unrelated slow-growing mutant (34) and from chloroquine-treated WT parasites ruled out a secondary effect of reduced parasite fitness or mortality on Hz morphology (*SI Appendix*, Fig. S2F and G).

To determine whether the crystalline order was affected by deregulation of PbPV5, we obtained electron diffraction patterns from WT- and *pv5::5'hsp101*-derived Hz (Fig. 2I) and analysed the maximum diffracted intensities in concentric bins as a function of resolution. There was no difference in the drop-off of diffracted intensity between WT and mutant and the peak positions of the maxima corresponded (Fig. 2J). Differences in the magnitude of individual peaks can be attributed to preferential orientation, especially of the *pv5::5'hsp101*-derived crystals, which most often come to lie at their {100} faces. Together, these data

indicate no differences in crystalline order or unit cell upon functional impairment of *PbPV5* and we conclude that altered crystal morphology is not caused by alternative nucleation into a different haematin polymorph. Thus, deregulation of *PbPV5* leads to the formation of ordered elongated Hz crystals with a highly variable and abnormal habit.

### **PV5 controls Hz branching in *P. falciparum***

To investigate the consequences of *PV5* disruption, we generated a conditional *PV5* knockout line of the human pathogen *P. falciparum*, allowing rapamycin-induced DiCre-mediated excision of the *PfPV5* gene (Fig. 3A and *SI Appendix*, Fig. S3A). Correct modification of the locus was indicated by diagnostic PCR and by the successful tagging of *PfPV5* with a 3xHA tag, as demonstrated by Western blot and immunofluorescence analysis (Fig. 3C and D and *SI Appendix*, Fig. S3B and C). As in *P. berghei*, tagged *PV5* localized to the PV and to intraparasitic vesicular structures in *P. falciparum*. No signal was observed within the central FV (*SI Appendix*, Fig. S3C).

Treatment of *pv5-3xHA:loxP* parasites with rapamycin led to efficient gene excision and complete loss of *PfPV5* protein expression during the same intraerythrocytic cycle (Fig. 3B-D). This did not detectably affect parasite maturation but did result in a modest merozoite invasion defect upon rupture of the *PfPV5*-null schizonts, reducing parasite replication (*SI Appendix*, Fig. S4A-C). Extended monitoring of the rapamycin-treated parasites showed that despite this ~40% fitness cost, *PfPV5* appeared to be dispensable for asexual blood stage growth *in vitro* (*SI Appendix*, Fig. S4B).

To examine the effects of *PfPV5* ablation on haem biomineralization, Hz released at parasite egress was examined by light microscopy of fixed Giemsa-stained culture smears. This revealed that in the absence of *PfPV5* Hz no longer formed clusters of separate elongated crystals, but rather appeared as aggregates which only occasionally fell apart into individual globular units (Fig. 3E). Accordingly, microscopic inspection of live parasites revealed that the characteristic twirling motion of Hz within the central FV was largely lost upon *PfPV5* knockout (Fig. 3F and *SI Appendix*, Movie S1).

The dramatic abnormalities in Hz crystal morphology resulting from ablation of *PfPV5* were even more evident by SEM analysis. While WT parasites formed crystals of the expected brick-like morphology, individual Hz units from rapamycin-treated *pv5-3xHA:loxP* parasites appeared smaller and more globular (Fig. 3G and *SI Appendix*, Table S1). The surfaces of these Hz units were covered in scales and stubby crystal buds. Individual crystals of comparable bud-like dimensions were not observed, indicating a branching rather than an aggregation phenomenon. In some instances, a lower number of crystal buds allowed the

visualization of an ordered Hz core, suggesting that branching is initiated from a regular parent crystal (Fig. 3G). We observed several morphological intermediates between slightly scaled Hz, highly branched crystal units and fused congregations (Fig. 3G). We frequently observed enormous aggregates of spherical proportions, mirroring the shape of the central FV (Fig. 3G). This suggested that hyperactive crystal branching in the absence of *PfPV5* caused individual studded Hz units to stick together and subsequently merge during Hz growth, which might explain the absence of motion in the parasite's FV (Fig. 3G). Non-rapamycin-treated *pv5-3xHA:loxP* control parasites mainly formed regular Hz crystals, however 27.5% of the crystals exhibited a modest degree of branching (Fig. 3G and *SI Appendix*, Table S1). Furthermore, crystal size and aspect ratio were reduced in comparison to WT parasites, together suggesting a moderate functional impairment of 3xHA-tagged *PfPV5* (Fig. 3G and *SI Appendix*, Table S1).

To determine whether *PfPV5* loss impacts on haemoglobin digestion, we examined the haemoglobin content of synchronous saponin-released *pv5-3xHA:loxP* parasites. We found that rings and trophozoites contained normal amounts of intraparasitic haemoglobin in the absence of *PfPV5* (*SI Appendix*, Fig. S5A). By contrast, *PfPV5*-deficient schizonts exhibited a ~2-fold increase in levels of haemoglobin. Despite this, we observed no vacuolar bloating as seen in parasites where haemoglobin catabolism is blocked by the protease inhibitor E64, suggesting that the slightly elevated haemoglobin levels in the absence of *PfPV5* fall within the range of residual substrate and do not contribute to the observed defects (*SI Appendix*, Fig. S5B). Furthermore, treatment of WT parasites with E64 produced no changes in the architecture of Hz (*SI Appendix*, Fig. S5C). Our data thus show that PV5 regulates Hz morphogenesis in *P. falciparum* independent of haemoglobin breakdown.

## **PbPV5 expression influences antimalarial drug sensitivity *in vivo***

In the light of our evidence implicating PV5 in Hz formation, we next tested whether parasites with affected PV5 function display altered sensitivity towards chloroquine, a 4-aminoquinoline which is thought to inhibit biomineralization in *Plasmodium* (22-25). The absence of *PfPV5* did not detectably alter chloroquine sensitivity in cultured *P. falciparum* parasites (*SI Appendix*, Fig. S4D). In stark contrast to this, however, the *P. berghei* promoter swap mutants responded to drug treatment slightly earlier and disappeared from the circulation much more rapidly than WT parasites (Fig. 4A). A similar phenotype was observed upon treatment of infected mice with the artemisinin derivative artesunate, also previously been implicated in haem sequestration, although this remains contentious (35-39) (Fig. 4B). Most surprisingly, we also observed marked hypersensitivity of the *P. berghei* mutants towards atovaquone, a compound that targets the parasite's mitochondrial electron transport chain (Fig. 4C), as well as a slight

290 but non-significant increase in sensitivity towards the antifolate sulfadoxin (Fig. 4D). The  
 291 relative survival levels of *pv5::5'ptex88* and *pv5::5'hsp101* on the fourth day of drug treatment  
 292 suggested the greatest degree of hypersensitivity towards chloroquine (2.1% and 1.4% of WT  
 293 survival, respectively), followed by atovaquone (3.5% and 8.6%) and artesunate (4.4% and  
 294 9.9%), and eventually sulfadoxin (20.5% and 27.8%). Collectively, these results suggest that  
 295 interference with *PV5* expression critically enhances vulnerability of the parasite towards drug-  
 296 mediated insult during *in vivo* blood infection.

## DISCUSSION

In this work, we have demonstrated that Hz formation in malaria parasites involves a secreted calycin family member called PV5. While transcriptional deregulation of *PV5* in *P. berghei* resulted in protracted Hz elongation along a pre-existing crystal plane, multidirectional branching was observed in the complete absence of PV5 in *P. falciparum*. Species differences aside, the disparity between those two phenotypes can be explained by the unique transcriptional dynamics observed in the *P. berghei* mutants. Here, the hyperactive crystal elongation, that follows an initial phase of normal Hz growth, coincides with a substantial increase in *PbPV5* transcript abundance during late parasite development. Together with the chaotic Hz crystal branching observed in PV5-deficient *P. falciparum* parasites, this leads us to propose that PV5 acts as a facilitator of unidirectional Hz extension.

It is interesting to speculate on the mechanisms by which PV5 may partake in haem biomineralization. In laboratory crystallization experiments, the extent of crystallographic mismatch branching is highly dependent on the degree of solute supersaturation, with high levels favouring the generation of novel crystal nuclei on the surface of the parent crystal (40). By contrast, lower degrees of supersaturation usually promote the expansion of pre-existing crystals (40). It is conceivable that PV5 might reduce the extent of haem supersaturation by binding haem or haematin dimers, thereby moderating *de novo* Hz nucleation and promoting unidirectional crystal elongation. This could explain the Hz branching upon loss of PV5 in *P. falciparum* as well as the prolonged crystal elongation and reduced Hz production upon late upregulation of *PV5* in the *P. berghei* mutants. In support of this model, some lipocalin family members are known to specifically bind the haem degradation product biliverdin (41-43). Such interactions are unlikely to occur within the predicted PV5  $\beta$ -barrel due to spatial constraints. However, although experimental validation for this is currently lacking, potential ligand binding sites might be located at the predicted prominently exposed loop between the barrel's  $\beta$ -strands 5 and 6 (Fig. 1B) or at the extended amino-terminus.

The crystal branching characterising PV5-deficient *P. falciparum* parasites could also be elicited by non-haem impurities adsorbing onto the crystal surface where they would generate novel nucleation sites (40). In this alternative functional model, PV5 could act to bind these impurities to create a vacuolar environment permissive for proper biomineralization. *PfPV5*-deficient parasites maintain an intact FV with a trans-vacuolar proton gradient as indicated by staining with the acidotropic dye Lysosensor Blue DND-167 (*SI Appendix*, Fig. S6A). In the absence of indications for FV membrane damage, differences in leakage of impurities from the parasite cytoplasm can be dismissed. However, we cannot rule out the

possibility that specific ions or organic compounds are more abundant in the vacuolar matrix of PV5-deficient parasites.

While the exact biophysical mechanisms that govern PV5-mediated Hz morphogenesis remain to be delineated, our results support a model of conventional crystallization within the aqueous milieu of the parasite's digestive compartments. The distinct changes in crystal morphology and branching behaviour in the PV5 mutants concur with established mineralogical phenomena and are difficult to reconcile with a lipid or protein-mediated polymerization scenario.

The striking dual localization pattern of PV5 is suggestive of initial secretion into the PV followed by endocytic uptake. Surprisingly, *PfPV5* did not ultimately localize to the Hz-containing FV in *P. falciparum*, but was frequently detected in intraparasitic vesicular structures. These vesicles likely reflect endosomal compartments, which have previously been implicated as sites of Hz nucleation and early crystal growth (44). The apparent exclusion of *PfPV5* from the FV might indicate recycling to the PV. We propose that the effects exerted by *PfPV5* in these organelles are eventually maintained within the FV upon endosomal fusion, where *PfPV5* activity is no longer required. The interdependency between early and late endosomal compartments is further supported by the observation of transient vacuolar swelling in the *P. berghei* mutants. Here, the inability to crystallize sufficient amounts of haem within the DVs might lead to a delay in DV budding, resulting in enlarged haemoglobin-containing FVs, and similar mechanisms are likely the cause for the residual haemoglobin in the FV of *PfPV5*-deficient *P. falciparum* schizonts. Accordingly, the Hz-inhibiting activities of aminoquinolines and artemisinin have been shown to be accompanied by an inhibition of endocytic trafficking and haemoglobin processing (45, 46).

Our previous experiments had indicated that *PbPV5* is essential for the asexual blood stage development of *P. berghei* (27), and the deregulation of *PbPV5* transcription in the mutants described here indeed led to a striking fitness cost during *in vivo* infection. By contrast, complete ablation of *PfPV5* in *P. falciparum* only resulted in a moderate fitness loss *in vitro*. The apparent dispensability of *PfPV5* is therefore puzzling, but can be resolved by the notion that *in vitro* culture does not necessarily reflect all adversities encountered during host infection. For instance, Hz-mediated stiffening of the residual body in the absence of PV5 might hinder the passage of infected cells through capillaries or through the inter-endothelial slits of the spleen, a scenario that would result in parasite elimination only during *in vivo* infection. Similarly, we observed enhanced drug susceptibility only in the *P. berghei* mutants. Thus, it appears plausible, that any imbalance in haem biomineralization in the absence of PV5 is compensated for under optimal culture conditions and unfolds its adverse effects only during *in vivo* infection. We thus propose that the molecular mechanism by which PV5

regulates Hz formation might involve host factors that are not encountered in a cell culture setting.

The observation of enhanced drug susceptibility in the PbPV5 mutants is in agreement with the notion that aberrant haem biomineralization chemo-sensitizes parasites to partner drugs. An attractive path for drug development would be the identification of specific PV5 inhibitors. Our results suggest that these would act synergistically with a range of antimalarials *in vivo*, as shown here by elevated parasite clearance rates during infection with the PbPV5 mutants. An unrelated slow-growing *P. berghei* mutant deficient in the maintenance of the mitochondrial membrane potential displayed normal sensitivity towards atovaquone using the same internally controlled assay (47), indicating that reduced parasite multiplication is unlikely to cause drug hypersensitivity. Although oxidative stress and lipid peroxidation remained unchanged upon deletion of PfPV5 (*SI Appendix*, Fig. S6B), the imbalance in haem biomineralization suggests abnormal haem concentrations within the parasite mediating the fitness loss and drug hypersensitivity.

Together, we provide the first conclusive evidence for a parasite factor involved in Hz formation *in vivo*, called PV5. Since this parasite-encoded member of the calycin superfamily also governs the parasites' vitality and susceptibility towards drug-mediated insult during blood infection, our observations reinforce Hz formation as an attractive pathway for therapeutic intervention with an emphasis on development of a universal synergistic partner drug for antimalarial combination therapies.

## MATERIALS & METHODS

**Structure homology modelling.** Structure homology modelling was performed using the SWISS-MODEL server (48). *PfPV5* (residues 35-214) was aligned to the experimentally validated structure of *EcBlc* (residues 27-175, PDB ID: 3MBT) (49), resulting in a GMQE value of 0.39 and a QMEAN value of -5.48. Modelling was confirmed with I-TASSER (50), which also identified *EcBlc* (PDB ID: 2ACO) (51) as the most closely related structural analogue of *PfPV5* with a TM score of 0.75. Due to a lack of sequence similarity, the structure of the extended *PfPV5* amino-terminus could not be modelled.

***P. berghei* cultivation.** *P. berghei* parasites were propagated in SWISS mice under constant drug pressure with pyrimethamine (70 mg/l in drinking water, ingested *ad libitum*, MP Biomedicals) to avoid homology-induced reversion of the promoter swap mutants to the original WT genotype. This was routinely checked by diagnostic PCR of genomic DNA as shown in *SI Appendix*, Figures S2 A and B. Drug pressure was withdrawn 5 days prior to experimentation to avoid secondary effects of pyrimethamine treatment. Pyrimethamine-resistant Berred WT parasites (52) were treated accordingly. All infection experiments were carried out in strict accordance with the German ‘Tierschutzgesetz in der Fassung vom 22. Juli 2009’ and the Directive 2010/63/EU of the European Parliament and Council ‘On the protection of animals used for scientific purposes’. The protocol was approved by the ethics committee of the Berlin state authority (‘Landesamt für Gesundheit und Soziales Berlin’, permit number G0294/15).

*P. berghei* growth was determined with the previously described intravital competition assay (52). In short, 500 mCherry-fluorescent Berred WT and 500 GFP-fluorescent mutant blood stage parasites were co-injected intravenously and parasitaemia was analysed daily by flow cytometry. For drug sensitivity assays,  $5 \times 10^6$  WT and  $5 \times 10^6$  mutant parasites were co-injected intravenously. Drug treatment as well as daily flow cytometric parasite detection were commenced three days later (47). Mice were treated with curative doses of chloroquine (288 mg/l in drinking water, ingested *ad libitum*, Sigma Aldrich), atovaquone (1.44 mg/kg body weight per day injected intraperitoneally; GlaxoSmithKline), artesunate (50 mg/kg body weight per day injected intraperitoneally; Sigma Aldrich) or sulfadoxin (1.4 g/l in drinking water, ingested *ad libitum*; Sigma Aldrich). Mixed blood stages and schizonts were purified by nycodenz gradient centrifugation (53).

***P. falciparum* cultivation.** *P. falciparum* parasites were propagated in type AB+ human red blood cells at 90% N<sub>2</sub>, 5% CO<sub>2</sub> and 5% O<sub>2</sub> at 37°C in RPMI 1640 containing AlbuMAXII

(Thermo Fisher Scientific) supplemented with 2 mM L-glutamine. Parasites were routinely synchronized using a combination of percoll gradient centrifugation and sorbitol lysis and were treated with 100 nM rapamycin, 21.7  $\mu$ M E64 or equivalent volumes of dimethyl sulfoxide (DMSO) from the early ring stage onward. Growth assays were performed as described previously (54) and parasitaemia as well as DNA content were measured by flow cytometry using the nuclear dye SYBR Green (1:10,000; Thermo Fisher Scientific). For invasion assays, mature schizonts were incubated at 2% initial parasitaemia under static or shaking (120 rpm) conditions, as confirmed by flow cytometry. Parasitaemia was measured again 24 hours after inoculation and the fold-change was calculated. For drug-response analysis of *pv5-3xHA:loxP* parasites, ring stage cultures at 0.5% parasitaemia were treated with varying concentrations of chloroquine in the presence of DMSO or rapamycin. Parasitaemia was determined three days later and the fold-change was calculated.

**Generation and validation of transgenic *Plasmodium* parasites.** To generate the PbPV5 promoter swap mutants, the amino-terminal sequence of PbPV5 (PBANKA\_0826700) was PCR-amplified and cloned into the B3D+ vector using *Bam*HI and *Sac*II. The promoters of PbPTEX88 (PBANKA\_0941300) or PbHSP101 (PBANKA\_0931200) were then amplified and cloned in front of the start codon using *Bam*HI (*SI Appendix*, Figure S1A). Vectors were linearized with *Bst*BI and transfected into GFP-fluorescent *P. berghei* Bergreen WT parasites, using standard protocols (53, 55, 56). Transgenic parasites were selected for with pyrimethamine and isolated by limiting dilution cloning. PbPV5 transcript abundance in the WT and the promoter swap mutants was measured by quantitative real-time PCR (qPCR) and normalized to *PbS18* rRNA.

The conditional PfPV5 knockout line was generated using established Cas9-mediated techniques. In short, *P. falciparum* 3D7 parasites constitutively expressing DiCre (B11 line) were co-transfected with a pDC2 guide plasmid inducing Cas9-mediated double strand cleavage of the PfPV5 locus (PF3D7\_0925900), together with a linearized repair template (57-59) (*SI Appendix*, Figure S3A). The template was generated by gene synthesis and contained 5' and 3' homology arms and a re-codonised 3xHA-tagged PfPV5 sequence. The endogenous intron of PfPV5 was replaced with an artificial intron containing a *loxP* site (58). A second *loxP* sequence was introduced behind the PfPV5 stop codon. Transgenic parasites were selected for with WR99210 and cloned by limiting dilution, making use of a previously developed plaque assay (60). Primers used for molecular cloning, diagnostic PCR, and qPCR are indicated in Figure 3A and in *SI Appendix*, Table S2 and Figures S1A and S3A.

**Fluorescence microscopy.** The transgenic *P. berghei* parasite line *pv5-tag-GFP<sup>PV</sup>* (27) was imaged live using an Axiomager Z2 epifluorescence microscope equipped with an AxioCam MR3 camera (Zeiss). For mechanical parasite expansion, 1-2  $\mu$ l of infected blood were incubated under a 22 x 40 mm coverslip for several minutes until erythrocyte lysis became apparent. *P. falciparum* *pv5-3xHA:loxP* parasites were fixed in 4% formaldehyde and imaged by immunofluorescence on an Eclipse Ni light microscope (Nikon) fitted with a C11440 digital camera (Hamamatsu). Immunofluorescence analysis was performed with rat anti-HA (1:500; Sigma Aldrich) and rabbit anti-SERA5 (1:500) (54) primary antibodies in combination with appropriate fluorophore-coupled secondary antibodies (1:1,000; Thermo Fisher Scientific). Stainings with Lysosensor Blue DND-167 (Thermo Fisher Scientific), BODIPY 581/591 C11 (Image-iT Lipid Peroxidation Kit, Thermo Fisher Scientific) and CellROX Green (Thermo Fisher Scientific) were performed according to the manufacturer's instructions.

**Scanning electron microscopy.** Hz was isolated from nycodenz (*P. berghei*) or percoll (*P. falciparum*) gradient-purified infected red blood cells. Cells were lysed in water at room temperature for 20 minutes, followed by a 10-minute centrifugation step at 17,000 x *g*. The pellet was resuspended in 2% SDS in water and centrifuged as above. Three more washing steps with 2% SDS were then followed by three washing steps with distilled water, before the crystals were resuspended and transferred onto round glass cover slips (12 mm), where they were dried. Cover slips were mounted on SEM specimen stubs, sputter-coated, and then imaged on a LEO 1430 (Zeiss) or on a Quanta FEG 250 scanning electron microscope (Thermo Fisher Scientific).

**Transmission electron microscopy.** Infected erythrocytes were initially fixed in 2.5% glutaraldehyde, embedded in beads of 2% agarose, fixed and contrasted with 1% osmium tetroxide, and further contrasted *en bloc* using 0.5% uranyl acetate. Following dehydration in a graded series of ethanol and propylene oxide, beads were embedded in epoxy resin and cured at 60°C for at least 24 hours. 60 nm sections were made with a Reichert Ultracut S ultramicrotome (Leica) using a diamond knife. Sections were retrieved on copper hexagonal mesh grids, and stained with 2% uranyl acetate and Reynold's lead citrate before imaging on an EM 900 transmission electron microscope (Zeiss) equipped with a wide-angle slow-scan 2K CCD camera (Tröndle Restlichtverstärkersysteme).

**Electron diffraction.** Purified Hz was added to glow-discharged Lacey carbon films on 400 mesh copper grids which were then transferred to a Vitrobot Mark IV plunge freezer (Thermo Fisher Scientific) with 100% humidity at 7 °C. The grids were blotted for 3 seconds with blot force 1 and plunge frozen in liquid ethane cooled by liquid nitrogen. Electron diffraction data

were collected on a Talos cryo-electron microscope (Thermo Fisher Scientific) operated at 200 keV equipped with a hybrid pixel Timepix detector (512 x 512 pixels, 55 x 55  $\mu\text{m}$  pixel size; Amsterdam Scientific Instruments). Still and rotation ( $70^\circ$ ) datasets were collected with a beam size of 2  $\mu\text{m}$ . The recording time varied between 15 and 100 seconds. To determine the resolution, a powder pattern of an aluminum diffraction standard was recorded.

Since the Hz crystals had a strong tendency to stick together, we measured diffraction data of crystal clusters. For each individual data set, we determined the location of the central electron beam and shifted the patterns to make the beams coincide. Since crystal clustering prevented indexing of the diffraction data, the radial median and maximum intensities were determined as a function of resolution. Hereafter, the WT and *pv5::5'hsp101* datasets were averaged and normalized to the local background median intensity at  $0.18 \text{ \AA}^{-1}$ .

**Subcellular fractionation and immunoblotting.** *P. falciparum* parasites were released from erythrocytes by treatment with 0.15% saponin in PBS and were lysed and heated in Laemmli buffer. Murine erythrocytes infected with the *pv5-tag-GFP<sup>PV</sup>* or *exp2-mCherry P. berghei* lines (61) were purified on a nycodenz gradient and lysed hypotonically for 1 hour on ice in 10 mM TRIS-HCl, pH 7.5. *P. berghei* lysates were spun 50 minutes at  $100,000 \times g$ . Membrane pellets were resuspended in 0.1 M  $\text{Na}_2\text{CO}_3$  in PBS or in 1% Triton X-100 in PBS, respectively, and spun 50 minutes at  $100,000 \times g$ . Equal amounts of these fractions and *pv5-3xHA:loxP* parasite lysates were separated on SDS-polyacrylamide and transferred onto a nitrocellulose membrane. Western blotting was performed using rat anti-mCherry (1:5,000; ChromoTek), chicken anti-GFP (1:5,000; Abcam), rat anti-HA (1:1,000, Sigma Aldrich), rat anti-PfBiP (1:1,000) (62) and rabbit anti-human-haemoglobin- $\alpha$  primary antibodies (1:1,000, Abcam) followed by chemiluminescence detection with horseradish peroxidase-coupled secondary antibodies (1:10,000; Sigma Aldrich, or 1:5,000, Jackson ImmunoResearch).

**Quantitative Hz analysis.** *P. berghei* Hz was visualized and quantified in methanol-fixed trophozoites by reflection contrast polarized light microscopy using a Leica DMR microscope equipped with a ProgRes MF camera (Jenoptik) and the POL filter set 513813 (Leica). Cellular granularity was approximated by quantification of side scattered light using an LSRFortessa flow cytometer (BD Biosciences). Hz crystal dimensions were analysed using FIJI. Due to the variation in the *P. berghei* mutant's crystal width, individual crystals were divided into nine evenly spaced segments along the dominant axis. The width of each segment was determined and the values were averaged. For the *pv5::5'hsp101* parent crystal and the crystal outgrowth, transects were drawn through the central axis of either structure and their shared angle was

520 determined. Hz movement within the FV of *pv5-3xHA:loxP* parasites was imaged live 36 hours  
521 following treatment with DMSO or rapamycin, respectively.

## 522 REFERENCES

- 523 1. A. G. Maier, K. Matuschewski, M. Zhang, M. Rug, *Plasmodium falciparum*. *Trends*  
524 *Parasitol* **35**, 481-482 (2019).
- 525 2. P. A. Sigala, D. E. Goldberg, The peculiarities and paradoxes of *Plasmodium* heme  
526 metabolism. *Annu Rev Microbiol* **68**, 259-278 (2014).
- 527 3. V. L. Lew, T. Tiffert, H. Ginsburg, Excess hemoglobin digestion and the osmotic  
528 stability of *Plasmodium falciparum*-infected red blood cells. *Blood* **101**, 4189-4194  
529 (2003).
- 530 4. D. E. Goldberg, A. F. Slater, A. Cerami, G. B. Henderson, Hemoglobin degradation in  
531 the malaria parasite *Plasmodium falciparum*: an ordered process in a unique organelle.  
532 *Proc Natl Acad Sci U S A* **87**, 2931-2935 (1990).
- 533 5. C. Slomianny, G. Prensier, P. Charet, [Comparative ultrastructural study of the process  
534 of hemoglobin degradation by *P. berghei* (Vincke and Lips, 1948) as a function of the  
535 state of maturity of the host cell]. *J Protozool* **32**, 1-5 (1985).
- 536 6. A. R. Dluzewski *et al.*, Formation of the food vacuole in *Plasmodium falciparum*: a  
537 potential role for the 19 kDa fragment of merozoite surface protein 1 (MSP1(19)). *PLoS*  
538 *One* **3**, e3085 (2008).
- 539 7. S. Kumar, U. Bandyopadhyay, Free heme toxicity and its detoxification systems in  
540 human. *Toxicol Lett* **157**, 175-188 (2005).
- 541 8. S. Pagola, P. W. Stephens, D. S. Bohle, A. D. Kosar, S. K. Madsen, The structure of  
542 malaria pigment beta-haematin. *Nature* **404**, 307-310 (2000).
- 543 9. A. F. Slater *et al.*, An iron-carboxylate bond links the heme units of malaria pigment.  
544 *Proc Natl Acad Sci U S A* **88**, 325-329 (1991).
- 545 10. I. Weissbuch, L. Leiserowitz, Interplay between malaria, crystalline hemozoin  
546 formation, and antimalarial drug action and design. *Chem Rev* **108**, 4899-4914 (2008).
- 547 11. M. Olivier, K. Van Den Ham, M. T. Shio, F. A. Kassa, S. Fougeray, Malarial pigment  
548 hemozoin and the innate inflammatory response. *Front Immunol* **5**, 25 (2014).
- 549 12. T. J. Egan, W. W. Mavuso, K. K. Ncokazi, The mechanism of beta-hematin formation  
550 in acetate solution. Parallels between hemozoin formation and biomineralization  
551 processes. *Biochemistry* **40**, 204-213 (2001).
- 552 13. T. J. Egan, D. C. Ross, P. A. Adams, Quinoline anti-malarial drugs inhibit spontaneous  
553 formation of beta-haematin (malaria pigment). *FEBS Lett* **352**, 54-57 (1994).
- 554 14. M. M. Chen, L. Shi, D. J. Sullivan, Jr., *Haemoproteus* and *Schistosoma* synthesize  
555 heme polymers similar to *Plasmodium* hemozoin and beta-hematin. *Mol Biochem*  
556 *Parasitol* **113**, 1-8 (2001).
- 557 15. A. Dom, R. Stoffel, H. Matile, A. Bubendorf, R. G. Ridley, Malarial haemozoin/beta-  
558 haematin supports haem polymerization in the absence of protein. *Nature* **374**, 269-  
559 271 (1995).
- 560 16. D. Jani *et al.*, HDP – a novel heme detoxification protein from the malaria parasite.  
561 *PLoS Pathog* **4**, e1000053 (2008).
- 562 17. D. J. Sullivan, Jr., I. Y. Gluzman, D. E. Goldberg, *Plasmodium* hemozoin formation  
563 mediated by histidine-rich proteins. *Science* **271**, 219-222 (1996).
- 564 18. A. F. Slater, A. Cerami, Inhibition by chloroquine of a novel haem polymerase enzyme  
565 activity in malaria trophozoites. *Nature* **355**, 167-169 (1992).

- 566 19. A. N. Hoang, R. D. Sandlin, A. Omar, T. J. Egan, D. W. Wright, The neutral lipid  
567 composition present in the digestive vacuole of *Plasmodium falciparum* concentrates  
568 heme and mediates beta-hematin formation with an unusually low activation energy.  
569 *Biochemistry* **49**, 10107-10116 (2010).
- 570 20. M. A. Ambele, T. J. Egan, Neutral lipids associated with haemozoin mediate efficient  
571 and rapid beta-haematin formation at physiological pH, temperature and ionic  
572 composition. *Malar J* **11**, 337 (2012).
- 573 21. J. M. Pisciotto *et al.*, The role of neutral lipid nanospheres in *Plasmodium falciparum*  
574 haem crystallization. *Biochem J* **402**, 197-204 (2007).
- 575 22. D. J. Sullivan, Jr., I. Y. Gluzman, D. G. Russell, D. E. Goldberg, On the molecular  
576 mechanism of chloroquine's antimalarial action. *Proc Natl Acad Sci U S A* **93**, 11865-  
577 11870 (1996).
- 578 23. K. N. Olafson, T. Q. Nguyen, J. D. Rimer, P. G. Vekilov, Antimalarials inhibit hematin  
579 crystallization by unique drug-surface site interactions. *Proc Natl Acad Sci U S A* **114**,  
580 7531-7536 (2017).
- 581 24. T. Herraiz, H. Guillen, D. Gonzalez-Pena, V. J. Aran, Antimalarial quinoline drugs  
582 inhibit beta-hematin and increase free hemin catalyzing peroxidative reactions and  
583 inhibition of cysteine proteases. *Sci Rep* **9**, 15398 (2019).
- 584 25. S. N. Cohen, K. O. Phifer, K. L. Yielding, Complex formation between chloroquine and  
585 ferrihaemic acid *in vitro*, and its effect on the antimalarial action of chloroquine. *Nature*  
586 **202**, 805-806 (1964).
- 587 26. U. D'Alessandro, H. Buttiens, History and importance of antimalarial drug resistance.  
588 *Trop Med Int Health* **6**, 845-848 (2001).
- 589 27. J. M. Matz, K. Matuschewski, An *in silico* down-scaling approach uncovers novel  
590 constituents of the *Plasmodium*-containing vacuole. *Sci Rep* **8**, 14055 (2018).
- 591 28. D. R. Flower, The lipocalin protein family: structure and function. *Biochem J* **318** ( Pt  
592 **1**), 1-14 (1996).
- 593 29. D. R. Flower, A. C. North, C. E. Sansom, The lipocalin protein family: structural and  
594 sequence overview. *Biochim Biophys Acta* **1482**, 9-24 (2000).
- 595 30. H. E. Bullen *et al.*, Biosynthesis, localization, and macromolecular arrangement of the  
596 *Plasmodium falciparum* translocon of exported proteins (PTEx). *J Biol Chem* **287**,  
597 7871-7884 (2012).
- 598 31. M. Morita *et al.*, PV1, a novel *Plasmodium falciparum* merozoite dense granule protein,  
599 interacts with exported protein in infected erythrocytes. *Sci Rep* **8**, 3696 (2018).
- 600 32. H. Iriko *et al.*, *Plasmodium falciparum* exported protein 1 is localized to dense granules  
601 in merozoites. *Parasitol Int* **67**, 637-639 (2018).
- 602 33. T. D. Otto *et al.*, A comprehensive evaluation of rodent malaria parasite genomes and  
603 gene expression. *BMC Biol* **12**, 86 (2014).
- 604 34. J. M. Matz *et al.*, *In vivo* function of PTEx88 in malaria parasite sequestration and  
605 virulence. *Eukaryot Cell* **14**, 528-534 (2015).
- 606 35. Y. L. Hong, Y. Z. Yang, S. R. Meshnick, The interaction of artemisinin with malarial  
607 hemozoin. *Mol Biochem Parasitol* **63**, 121-128 (1994).
- 608 36. R. K. Haynes *et al.*, Artemisinin antimalarials do not inhibit hemozoin formation.  
609 *Antimicrob Agents Chemother* **47**, 1175 (2003).

- 610 37. W. Asawamahasakda, I. Ittarat, C. C. Chang, P. McElroy, S. R. Meshnick, Effects of  
611 antimalarials and protease inhibitors on plasmodial hemozoin production. *Mol*  
612 *Biochem Parasitol* **67**, 183-191 (1994).
- 613 38. A. V. Pandey, B. L. Tekwani, R. L. Singh, V. S. Chauhan, Artemisinin, an endoperoxide  
614 antimalarial, disrupts the hemoglobin catabolism and heme detoxification systems in  
615 malarial parasite. *J Biol Chem* **274**, 19383-19388 (1999).
- 616 39. N. Basilico, E. Pagani, D. Monti, P. Oliaro, D. Taramelli, A microtitre-based method  
617 for measuring the haem polymerization inhibitory activity (HPIA) of antimalarial drugs.  
618 *J Antimicrob Chemother* **42**, 55-60 (1998).
- 619 40. X. Y. Liu, "Heterogeneous nucleation and crystal network formation" in Crystal growth  
620 of technologically important electronic materials, K. Byrappa, T. Ohachi, H. Klapper,  
621 R. Fornari, Eds. (Allied Publishers PVT. Limited, New Delhi, 2003), pp. 118-135.
- 622 41. R. Huber *et al.*, Molecular structure of the bilin binding protein (BBP) from *Pieris*  
623 *brassicae* after refinement at 2.0 Å resolution. *J Mol Biol* **198**, 499-513 (1987).
- 624 42. R. Huber *et al.*, Crystallization, crystal structure analysis and preliminary molecular  
625 model of the bilin binding protein from the insect *Pieris brassicae*. *J Mol Biol* **195**, 423-  
626 434 (1987).
- 627 43. H. M. Holden, W. R. Rypniewski, J. H. Law, I. Rayment, The molecular structure of  
628 insecticyanin from the tobacco hornworm *Manduca sexta* L. at 2.6 Å resolution. *EMBO*  
629 *J* **6**, 1565-1570 (1987).
- 630 44. N. Abu Bakar, N. Klonis, E. Hanssen, C. Chan, L. Tilley, Digestive-vacuole genesis  
631 and endocytic processes in the early intraerythrocytic stages of *Plasmodium*  
632 *falciparum*. *J Cell Sci* **123**, 441-450 (2010).
- 633 45. Y. Zhang, Inhibition of hemoglobin degradation in *Plasmodium falciparum* by  
634 chloroquine and ammonium chloride. *Exp Parasitol* **64**, 322-327 (1987).
- 635 46. H. C. Hoppe *et al.*, Antimalarial quinolines and artemisinin inhibit endocytosis in  
636 *Plasmodium falciparum*. *Antimicrob Agents Chemother* **48**, 2370-2378 (2004).
- 637 47. J. M. Matz, C. Goosmann, K. Matuschewski, T. W. A. Kooij, An unusual prohibitin  
638 regulates malaria parasite mitochondrial membrane potential. *Cell Rep* **23**, 756-767  
639 (2018).
- 640 48. A. Waterhouse *et al.*, SWISS-MODEL: homology modelling of protein structures and  
641 complexes. *Nucleic Acids Res* **46**, W296-W303 (2018).
- 642 49. A. Schiefner, L. Chatwell, D. A. Breustedt, A. Skerra, Structural and biochemical  
643 analyses reveal a monomeric state of the bacterial lipocalin Blc. *Acta Crystallogr D Biol*  
644 *Crystallogr* **66**, 1308-1315 (2010).
- 645 50. J. Yang, Y. Zhang, Protein structure and function prediction using I-TASSER. *Curr*  
646 *Protoc Bioinformatics* **52**, 5 8 1-5 8 15 (2015).
- 647 51. V. Campanacci, R. E. Bishop, S. Blangy, M. Tegoni, C. Cambillau, The membrane  
648 bound bacterial lipocalin Blc is a functional dimer with binding preference for  
649 lysophospholipids. *FEBS Lett* **580**, 4877-4883 (2006).
- 650 52. J. M. Matz, K. Matuschewski, T. W. Kooij, Two putative protein export regulators  
651 promote *Plasmodium* blood stage development *in vivo*. *Mol Biochem Parasitol* **191**,  
652 44-52 (2013).
- 653 53. C. J. Janse *et al.*, High efficiency transfection of *Plasmodium berghei* facilitates novel  
654 selection procedures. *Mol Biochem Parasitol* **145**, 60-70 (2006).
- 655 54. R. Stallmach *et al.*, *Plasmodium falciparum* SERA5 plays a non-enzymatic role in the  
656 malarial asexual blood-stage lifecycle. *Mol Microbiol* **96**, 368-387 (2015).

- 657 55. J. M. Matz, T. W. Kooij, Towards genome-wide experimental genetics in the *in vivo*  
658 malaria model parasite *Plasmodium berghei*. *Pathog Glob Health* **109**, 46-60 (2015).
- 659 56. T. W. Kooij, M. M. Rauch, K. Matuschewski, Expansion of experimental genetics  
660 approaches for *Plasmodium berghei* with versatile transfection vectors. *Mol Biochem*  
661 *Parasitol* **185**, 19-26 (2012).
- 662 57. C. R. Collins *et al.*, Robust inducible Cre recombinase activity in the human malaria  
663 parasite *Plasmodium falciparum* enables efficient gene deletion within a single asexual  
664 erythrocytic growth cycle. *Mol Microbiol* **88**, 687-701 (2013).
- 665 58. M. L. Jones *et al.*, A versatile strategy for rapid conditional genome engineering using  
666 *loxP* sites in a small synthetic intron in *Plasmodium falciparum*. *Sci Rep* **6**, 21800  
667 (2016).
- 668 59. E. Knuepfer, M. Napiorkowska, C. van Ooij, A. A. Holder, Generating conditional gene  
669 knockouts in *Plasmodium* – a toolkit to produce stable DiCre recombinase-expressing  
670 parasite lines using CRISPR/Cas9. *Sci Rep* **7**, 3881 (2017).
- 671 60. J. A. Thomas *et al.*, Development and application of a simple plaque assay for the  
672 human malaria parasite *Plasmodium falciparum*. *PLoS One* **11**, e0157873 (2016).
- 673 61. J. M. Matz *et al.*, The *Plasmodium berghei* translocon of exported proteins reveals  
674 spatiotemporal dynamics of tubular extensions. *Sci Rep* **5**, 12532 (2015).
- 675 62. E. Knuepfer *et al.*, RON12, a novel *Plasmodium*-specific rhoptry neck protein important  
676 for parasite proliferation. *Cell Microbiol* **16**, 657-672 (2014).
- 677 63. R. Buller, M. L. Peterson, Ö. Almarsson, L. Leiserowitz, Quinoline binding site on  
678 malaria pigment crystal: a rational pathway for antimalaria drug design. *Cryst Growth*  
679 *Des* **2**, 553-562 (2002).
- 680 64. J. Friesen *et al.*, Natural immunization against malaria: causal prophylaxis with  
681 antibiotics. *Sci Transl Med* **2**, 40ra49 (2010).

## AUTHOR CONTRIBUTIONS

JMM conceived the study and performed all experiments requiring genetic manipulation and cultivation of *P. berghei* and *P. falciparum* parasites. JMM, BD, AB, PM, TS and LC contributed to Hz analysis by SEM and TEM. TBB, EvG and JPA performed and analysed electron diffraction experiments. KM and MJB contributed to data interpretation. The manuscript was written by JMM with input from TBB, EvG, JPA, KM and MJB.

## ACKNOWLEDGEMENTS

We thank Volker Brinkmann and Christian Goosmann (Max Planck Institute for Infection Biology, Berlin) for assistance with reflection contrast polarized light microscopy and Darren Flower (Aston University, Birmingham) and Leslie Leiserowitz (Weizmann Institute of Science, Rehovot) for fruitful discussion. This work was supported by a stipend from the Deutsche Forschungsgemeinschaft (DFG, project number 419345764 to JMM) and in part by funding to JMM, LC, AB and MJB from the Francis Crick Institute, which receives its core funding from Cancer Research UK (FC001043), the UK Medical Research Council (FC001043), and the Wellcome Trust (FC001043). JMM, BD, PM, TS and KM were also supported by the Humboldt University and by the Alliance Berlin Canberra “Crossing Boundaries: Molecular Interactions in Malaria”, which is co-funded by a grant from the DFG for the International Research Training Group (IRTG) 2290 and the Australian National University. We further acknowledge funding from the Swiss National Science Foundation (project 31003A\_17002 to TBB and project 200021\_165669 to TBB and JPA). We thank the Center for Cellular Imaging and NanoAnalytics for support and use of the cryo-electron microscope.

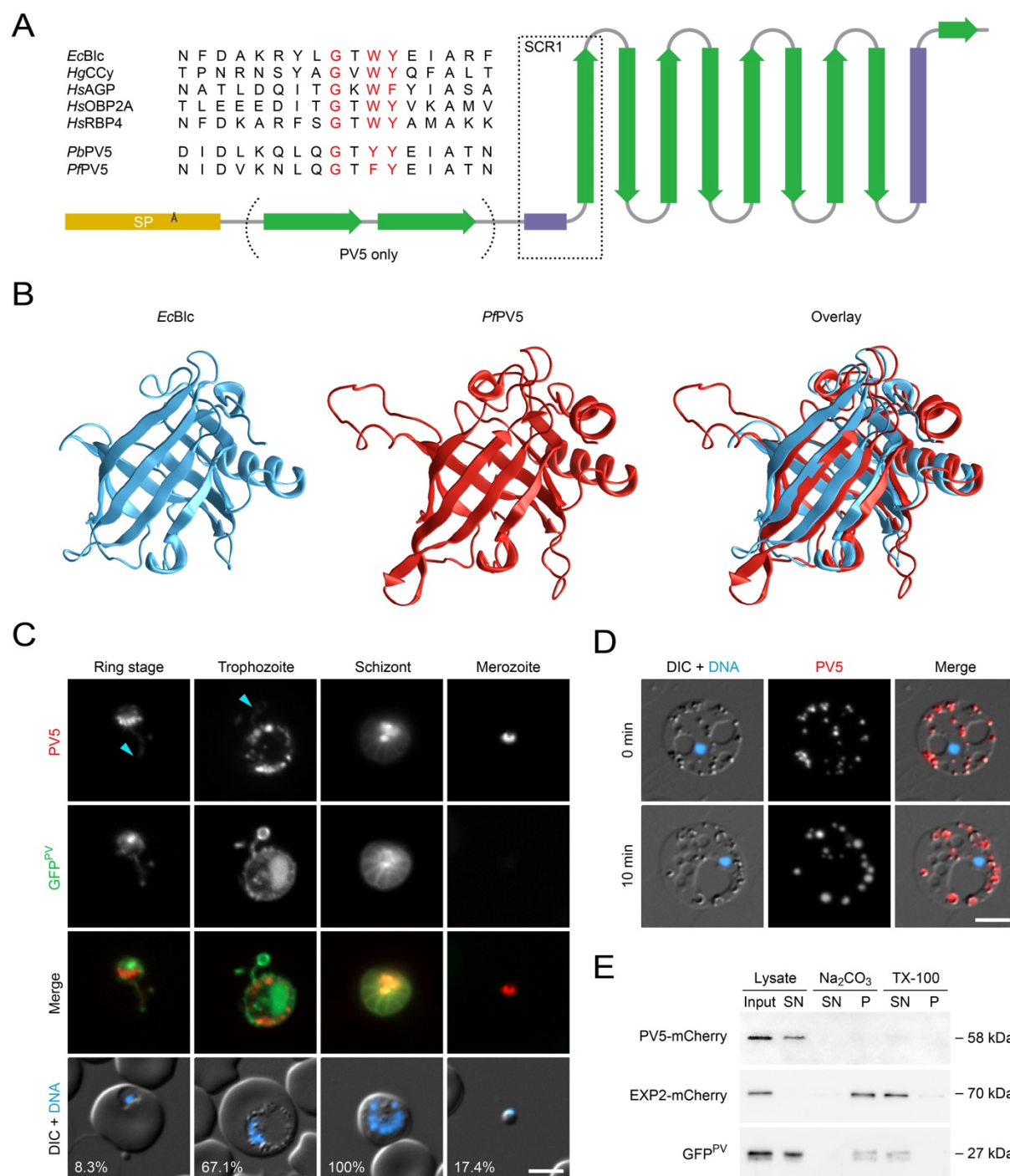


**Fig. 1.** The soluble lipocalin family member PV5 is trafficked to digestive vesicles in *Plasmodium berghei*.

(A) PV5 is a lipocalin family member. Secondary structure of *Plasmodium* PV5. Yellow, signal peptide (SP); green,  $\beta$ -strands; purple,  $\alpha$ -helices. Note the two amino-terminal  $\beta$ -strands specific to PV5. Alignments of the structurally conserved region 1 (SCR1) from different lipocalin family members and PV5 are shown in the upper left corner. Signature residues are highlighted in red. *EcBlc*, *Escherichia coli* bacterial lipocalin; *HgCCy*, *Homarus gammarus* (European lobster) crustacyanin; *HsAGP*, *Homo sapiens*  $\alpha_1$ -acid glycoprotein;

*HsOBP2A*, *H. sapiens* odorant-binding protein 2A; *HsRBP4*, *H. sapiens* retinol-binding protein 4; *Pb/PfPV5*, PV5 from *P. berghei* and *P. falciparum*.

(B) Structure homology modelling predicts a lipocalin fold for *PfPV5*. Shown are the experimentally validated structure of *EcBlc* (blue, left, residues 27-175, PDB ID: 3MBT), the derived model of *PfPV5* (red, centre, residues 35-214) using *EcBlc* as a homology template, and an overlay (right). Modelling was performed with SWISS-MODEL and supported by I-TASSER. Amino acid sequence identity is 20%, similarity calculated from BLOSUM62 substitution matrix is 0.3.

(C) Dual protein localization of *PbPV5* to extensions of the parasitophorous vacuole (PV) and to intraparasitic structures. Transgenic *P. berghei* parasites expressing the PV marker GFP<sup>PV</sup> and the endogenous *PbPV5* gene fused to mCherry-3xMyc were imaged live (27). Shown are the mCherry (first row) and GFP channels (second row), a merge of both signals (third row) and a merge of differential interference contrast images (DIC) and Hoechst 33342 nuclear stain (fourth row). Cyan arrowheads, *PbPV5* in PV tubules. Numbers represent normalized mCherry intensity values obtained by quantitative live fluorescence microscopy. N=44 parasites.

(D) Intraparasitic *PbPV5* localizes to Hz-containing digestive vesicles (DVs). Parasites were incubated in 1-2  $\mu$ l under a large coverslip (22 x 40 mm) for several minutes, leading to lysis of the host erythrocyte and the PV, and to mechanical expansion of the parasite (top). Shown are a merge of differential interference contrast and Hoechst 33342 nuclear stain (first row), the signal of tagged *PbPV5* (second row), as well as a merge of all three channels (third row). Swelling of *PbPV5*-containing DVs was observed ten minutes later (bottom). Note the even distribution of *PbPV5* throughout the swollen DVs. Bars, 5  $\mu$ m.

(E) *PbPV5* is a soluble protein. Subcellular fractionation was performed using the *PbPV5*-tagged parasite line, which also expresses the soluble marker GFP<sup>PV</sup>, and a *P. berghei* line expressing the transmembrane protein *PbEXP2* fused to mCherry-3xMyc (61). Cell lysates were centrifuged and resultant membrane pellets were subjected to solubilization with Na<sub>2</sub>CO<sub>3</sub> and Triton X-100 (TX-100). Input, supernatant (SN) and pellet fractions (P) were analysed by Western blot using anti-mCherry and anti-GFP primary antibodies.

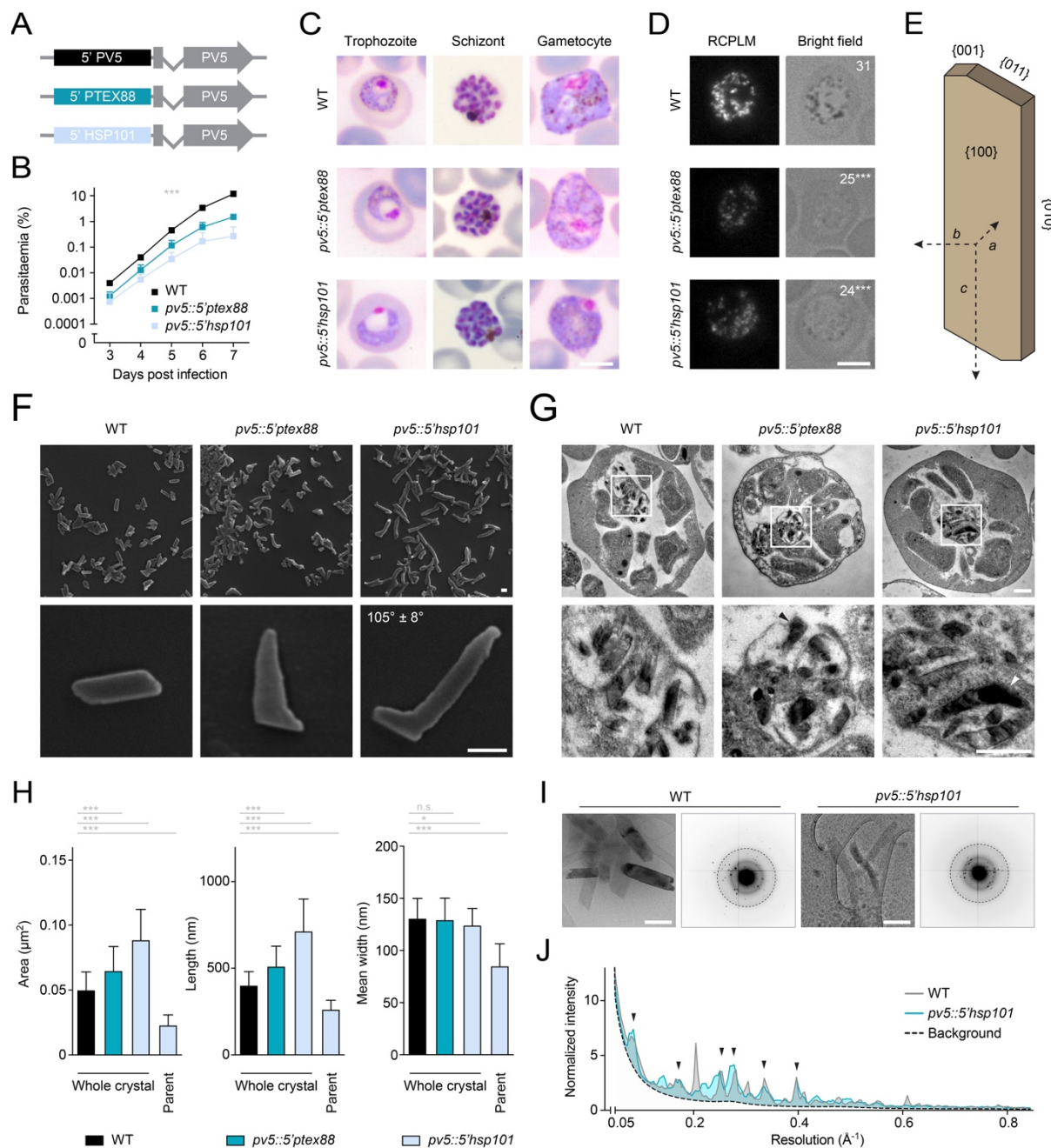


**Fig. 2.** Deregulated expression of *PV5* impacts haemozoin formation in *Plasmodium berghei*.

(A) Schematic representation of the genotypes of WT (top) and transgenic *pv5::5'ptex88* (middle) and *pv5::5'hsp101* parasites (bottom). In the mutants, the endogenous *PbPV5* promoter (black) was exchanged for the promoter of *PbPTEX88* (dark blue) or *PbHSP101* (light blue) respectively.

(B) Reduced parasite proliferation upon *PbPV5* promoter swapping. Asexual blood stage development was analysed using the intravital competition assay (52). Average parasite multiplication rates were 11.4 (WT), 9.1 (*pv5::5'ptex88*) and 6.2 (*pv5::5'hsp101*). Shown are mean values  $\pm$  SD. \*\*\*,  $P < 0.001$ ; Two-way ANOVA.  $N = 3$  independent infections.

(C) Morphology of trophozoite, schizont and gametocyte stages in the WT, *pv5::5'ptex88* and *pv5::5'hsp101* lines as observed by Giemsa staining. Note the lack of prominent dark pigment granules in mutant trophozoites and gametocytes as well as the dilation of the central food vacuole in mutant trophozoites. Bar, 5  $\mu$ m.

(D) PbPV5 is required for efficient Hz formation. Trophozoites were visualized by reflection contrast polarized light microscopy (RCPLM, left) and bright field imaging (right). Numbers indicate the mean quantity of bright puncta in RCPLM images. Significances are shown for the comparison of the mutants with WT. Bar, 5  $\mu$ m. See also *SI Appendix*, Fig. S2C.

(E) Hz crystal architecture. In *Plasmodium* WT parasites, Hz assembles as triclinic high aspect ratio parallelograms (63). Characteristic crystal axes and faces are indicated.

(F) Scanning electron micrographs of Hz purified from WT, *pv5::5'ptex88* and *pv5::5'hsp101* mixed blood stage parasites. The angle between the regularly shaped *pv5::5'hsp101* parent crystal and the outgrowth is indicated. N=130 crystals. Bars, 100 nm.

(G) Crystal morphology *in situ*. Shown are TEM images of WT, *pv5::5'ptex88* and *pv5::5'hsp101* schizonts (top) as well as their residual body at higher magnification (bottom). Abnormal crystal shapes in the mutants are indicated by arrowheads. Bars, 500 nm.

(H) Hyperactive Hz growth is unidirectional. Shown are the dimensions of whole individual Hz crystals extracted from WT, *pv5::5'ptex88* and *pv5::5'hsp101* parasites including the area exposed to the electron beam (left) as well as the length (centre) and mean width of the crystals (right). The theoretical dimensions of the *pv5::5'hsp101* parent crystal were interpolated and are depicted as well. n.s., non-significant; \*,  $P<0.05$ ; \*\*\*,  $P<0.001$ ; One-way ANOVA and Tukey's multiple comparison test. N=100 crystals.

(I, J) Unaltered crystalline order in Hz of *pv5::5'hsp101* parasites. (I) Depicted are TEM images (left) of Hz purified from WT and *pv5::5'hsp101* parasites as well as their corresponding electron diffraction patterns (right) showing comparable resolution of the Bragg peaks. Dashed circles demark a resolution of 0.5  $\text{\AA}^{-1}$ . Bars, 200 nm. (J) Plot of the radial maximum diffracted intensity as a function of resolution. Data were normalized to the average median intensity at 0.18  $\text{\AA}^{-1}$ , in order to correct for differences in diffracted volume. Arrowheads denote overlapping peaks. N=10 (WT) and 18 (*pv5::5'hsp101*) diffraction data sets.

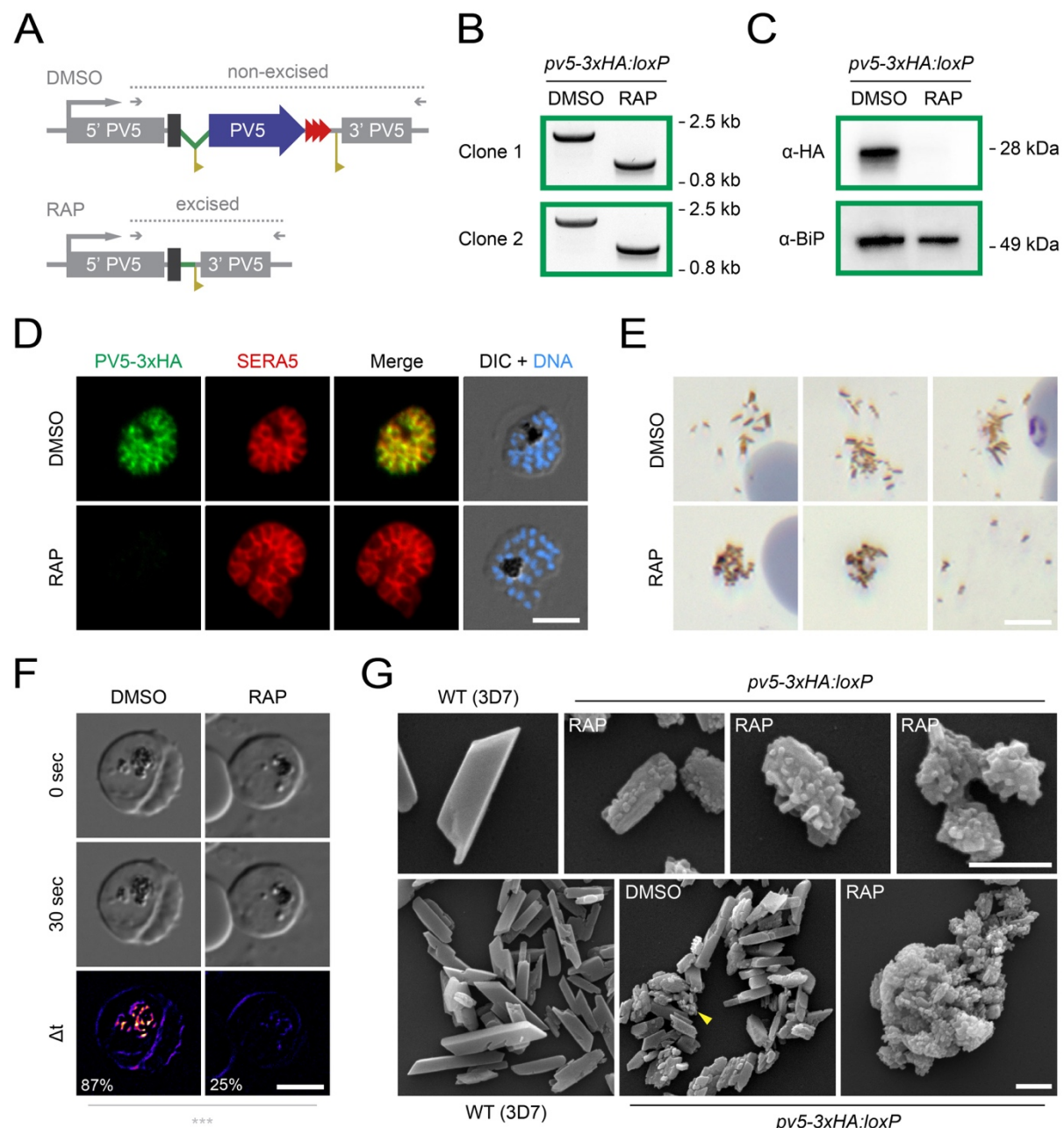


**Fig. 3.** Absence of PV5 causes haemozoin branching in *Plasmodium falciparum*.

(A) Schematic representation of DiCre-mediated *PfPV5* excision. The endogenous locus was modified to introduce *loxP* sites (yellow) flanking the majority of the coding sequence of the 3xHA (red)-tagged *PfPV5* (blue). The artificial intron is indicated in green. See also *SI Appendix*, Fig. S3A. Treatment with rapamycin (RAP) induces Cre recombinase-mediated excision of the *loxP*-flanked sequence which results in truncation of *PfPV5* leaving behind only the sequence encoding the protein's signal peptide. Excision-sensitive primer combinations are indicated by arrows and expected diagnostic PCR fragments by dotted lines.

(B) Diagnostic PCR of the *PfPV5* locus following treatment with dimethyl sulfoxide (DMSO)

or RAP, respectively, using the primer combinations depicted in A. Results are shown from two independent *pv5::3xHA:loxP* clones.

(C, D) Loss of *PfPV5* protein. (C) Western blot analysis of parasite extracts following treatment with DMSO or RAP, respectively, using anti-HA and anti-*PfBiP* primary antibodies. (D) Immunofluorescence analysis was performed with primary antibodies directed against HA and the PV protein *PfSERA5*. Shown are the individual signals of tagged *PfPV5* (green, first row) and *PfSERA5* (red, second row), a merge of both signals (third row) as well as a merge of differential interference contrast images (DIC) with Hoechst 33342 nuclear stain (fourth row) following treatment with DMSO or RAP, respectively. Bar, 5  $\mu$ m.

(E) Abnormal Hz morphology in the absence of *PfPV5*. Hz released from residual bodies during parasite egress was imaged in Giemsa-stained thin culture smears of DMSO and RAP-treated *pv5::3xHA:loxP* parasites. Note the spreading of elongated Hz crystals in DMSO-treated cultures and the clumping of granular Hz upon RAP treatment. Only in very few instances did the crystals detach from one another in RAP-treated cultures (last panel). Bar, 5  $\mu$ m.

(F) Reduced Hz movement in the digestive vacuole upon loss of *PfPV5*. Shown are DIC images of live DMSO and RAP-treated *pv5::3xHA:loxP* parasites 36 hours after invasion. Parasites were imaged twice at an interval of 30 seconds (top and centre) and the difference of both images visualized with pixel-by-pixel intensity subtraction (bottom). Note the absence of Hz movement in the RAP-treated parasite (see also *SI Appendix*, Movie S1). The percentage of parasites with moving Hz is indicated. \*\*\*,  $P < 0.001$ ; Student's *t*-test. N=4 independent experiments with >300 parasites each. Bar, 5  $\mu$ m.

(G) Scanning electron micrographs of Hz purified from WT and from DMSO or RAP-treated *pv5::3xHA:loxP* schizonts. Bars, 500 nm.

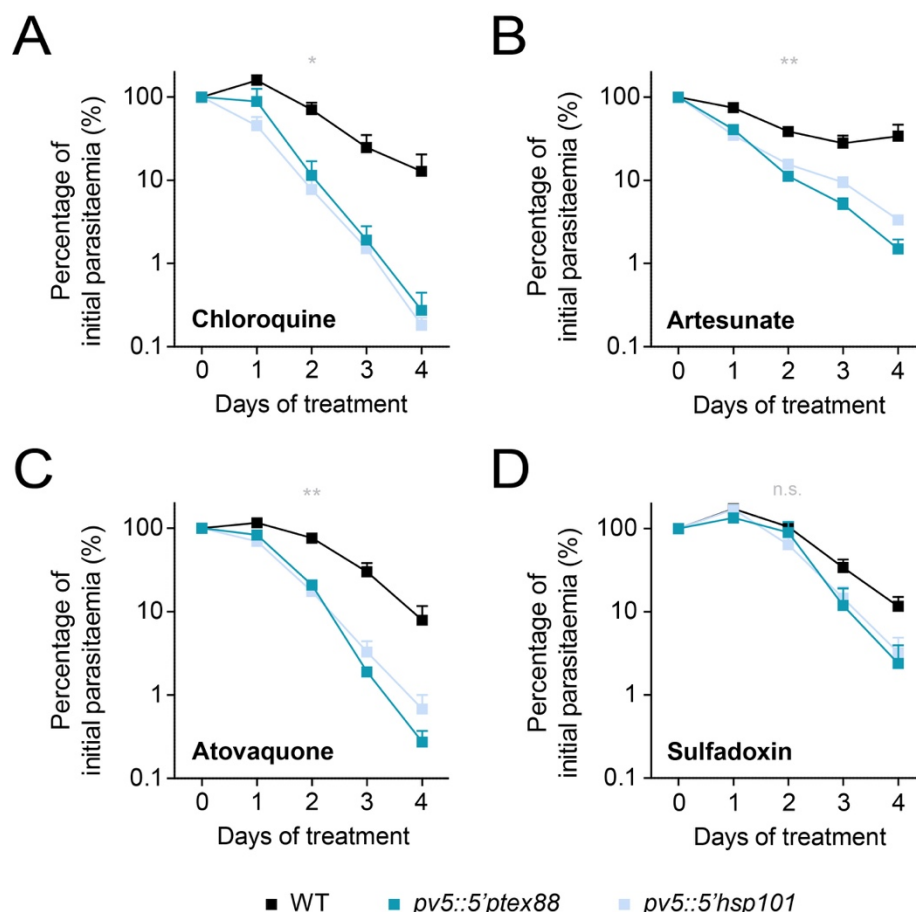


**Fig. 4.** Targeting PbPV5 function results in parasite hypersensitivity towards antimalarial drugs *in vivo*.

(A-D)  $5 \times 10^6$  mCherry-fluorescent *P. berghei* WT parasites were injected into SWISS mice together with  $5 \times 10^6$  GFP-fluorescent *pv5::5'ptex88* or *pv5::5'hsp101* parasites, respectively. From day three onward, mice were treated with curative doses of (A) chloroquine (288 mg/l in drinking water, *ad libitum*), (B) artesunate (50 mg/kg body weight, i.p.), (C) atovaquone (1.44 mg/kg body weight, i.p.) or (D) sulfadoxin (1.4 g/l in drinking water, *ad libitum*) and the respective parasitaemias were determined daily by flow cytometry of peripheral blood (47). Values are normalized to the parasitaemias on day 0 of treatment. Shown are mean values  $\pm$  SEM. n.s., non-significant; \*,  $P < 0.05$ ; \*\*,  $P < 0.01$ ; Two-way ANOVA. N=3 independent infections.

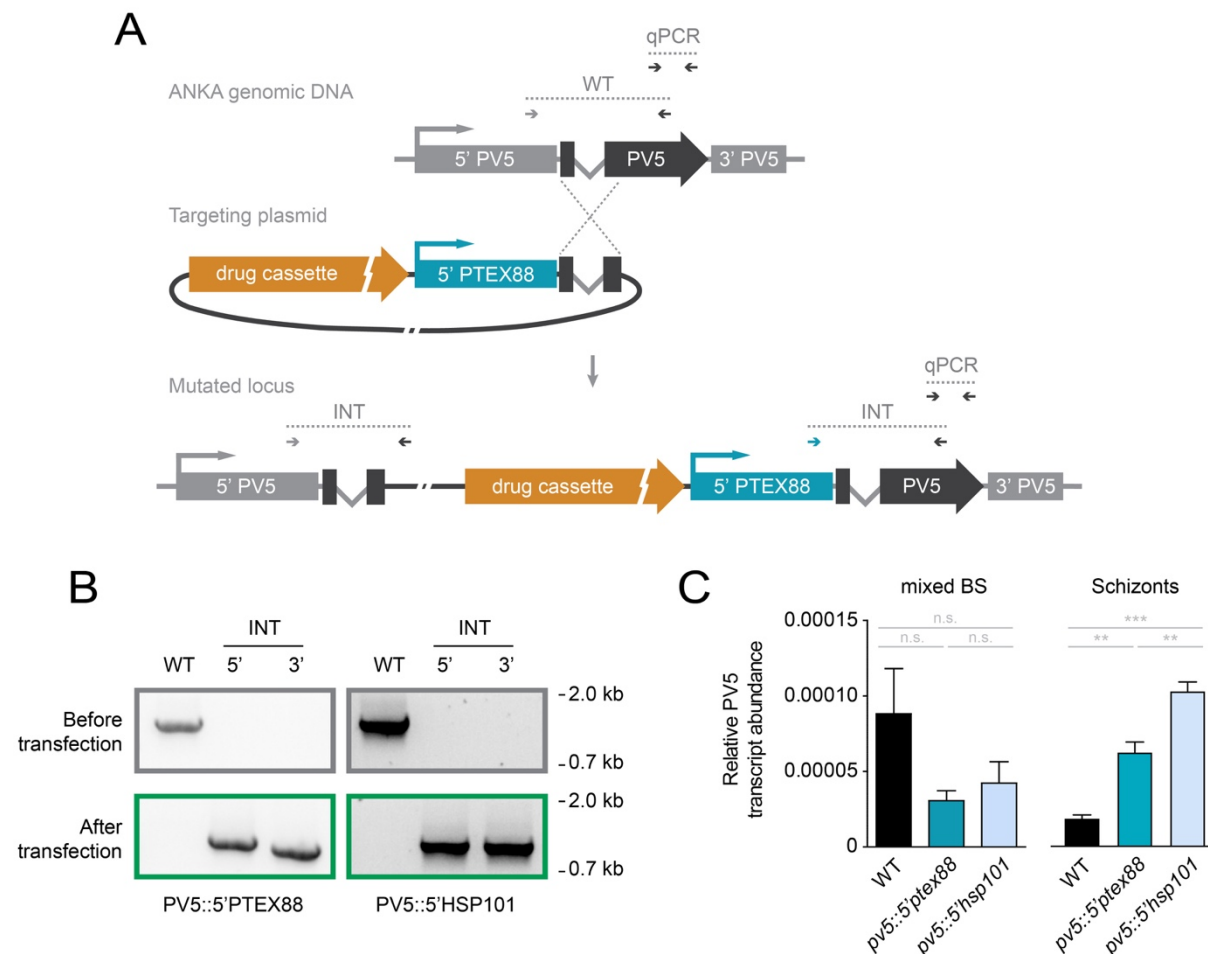


**Fig. S1.** Generation and validation of PbPV5 promoter swap mutants.

(A) Genetic strategy to exchange the endogenous promoter (light grey) of PbPV5 (dark grey) using single homologous recombination. The endogenous PbPV5 locus was targeted with an insertion plasmid containing the promoter sequence of PbPTEX88 (shown, blue) or PbHSP101 (not shown) fused to the amino-terminal sequence of PbPV5 as well as the drug-selectable hDHFR-yFcu cassette (orange). Successful insertion yields parasites expressing full length PbPV5 from a heterologous promoter and a non-functional amino-terminal fragment from the endogenous promoter, encoding the PbPV5 signal peptide. Primer combinations for wild-type (WT) and integration-specific reactions (INT) as well as for quantitative real-time PCR (qPCR) are indicated by arrows and expected amplicons by dotted lines.

(B) Diagnostic PCR of the WT locus (top) and of the drug-selected and isolated PbPV5 mutants (bottom) using the primer combinations depicted in A.

(C) Dynamic changes in PbPV5 transcription upon promoter swap. Mixed blood stages (BS) and mature segmented schizonts were purified from mouse blood or from *in vitro* culture, respectively, and subjected to qPCR using primers targeting a carboxy-terminal portion of

842 *PbPV5*, as depicted in A. *PbPV5* transcript abundance was normalized to *Pb18S* rRNA.  
843 Shown are mean values  $\pm$  SEM. n.s., non-significant; \*\*,  $P < 0.01$ ; \*\*\*,  $P < 0.001$ ; One-way  
844 ANOVA and Tukey's multiple comparison test. N=6 for mixed blood stages and 3 for schizonts.

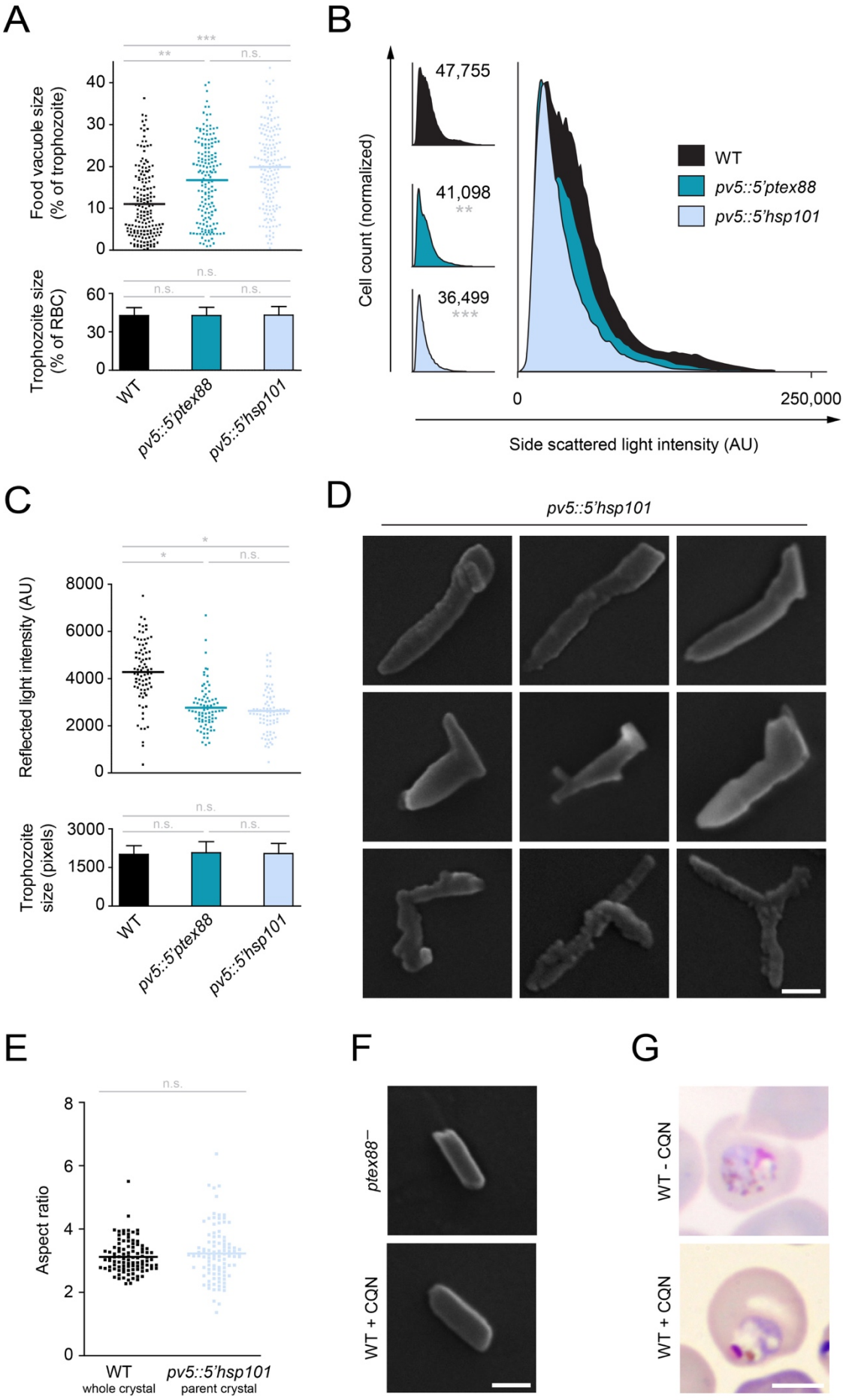


**Fig. S2. Vacuolar dilation and defective haemozoin formation in the PbPV5 mutants.**

(A) Quantification of vacuolar dilation. The translucent area observed in Giemsa-stained trophozoites corresponding to the food vacuole was measured microscopically and expressed as the percentage of the entire trophozoite area (upper graph). Depicted are individual and mean values (bars). Only trophozoites of identical size were analysed (lower graph). Shown are mean values  $\pm$  SD. n.s., non-significant; \*\*,  $P < 0.01$ ; \*\*\*,  $P < 0.001$ ; One-way ANOVA and Tukey's multiple comparison test. N=165 trophozoites from 5 independent infections.

(B) PbPV5 promoter swap mutants are less granular. Infected blood was subjected to flow cytometry and the intensity of the side scattered light was determined. Shown are individual histograms including the mean side scatter intensity values (left) as well as a merge of WT, *pv5::5'ptex88* and *pv5::5'hsp101* histograms (right). Significances are shown for the comparison of the mutants with WT. n.s., non-significant; \*\*,  $P < 0.01$ ; \*\*\*,  $P < 0.001$ ; One-way ANOVA and Tukey's multiple comparison test. N=6 independent infections.

(C) Quantitative reflection contrast polarized light microscopy. Depicted are individual and mean intensity values of reflected light in methanol-fixed WT, *pv5::5'ptex88* and *pv5::5'hsp101* trophozoites (bars, upper graph). Only trophozoites of similar size were analysed (lower graph). Depicted are mean values  $\pm$  SD. n.s., non-significant; \*,  $P < 0.05$ ; One-way ANOVA and Tukey's multiple comparison test. N=80 trophozoites from 4 independent infections.

(D) A selection of Hz crystals generated by *pv5::5'hsp101* parasites as visualized by scanning electron microscopy. Bar, 100 nm.

(E) Normal aspect ratio of *pv5::5'hsp101* parent crystals. Shown are the aspect ratios of whole Hz crystals from WT parasites and of the parent crystal from *pv5::5'hsp101*-generated Hz. Depicted are individual and mean values (bars). n.s., non-significant; Student's *t*-test. N=100 crystals.

(F, G) Hz morphology is not affected by slow parasite growth or mortality. (F) Crystals were extracted from slow-growing *PTEX88* knockout parasites (top) and from WT parasites treated with curative doses of chloroquine (CQN, 288 mg/l in drinking water, *ad libitum*) (bottom) and were visualized by scanning electron microscopy. Bar, 100 nm. (G) Morphology of untreated (top) and CQN-treated WT parasites (bottom) as shown by Giemsa staining. Note the pigment clumping and vesiculation in the dying parasite. Bar, 5  $\mu$ m.

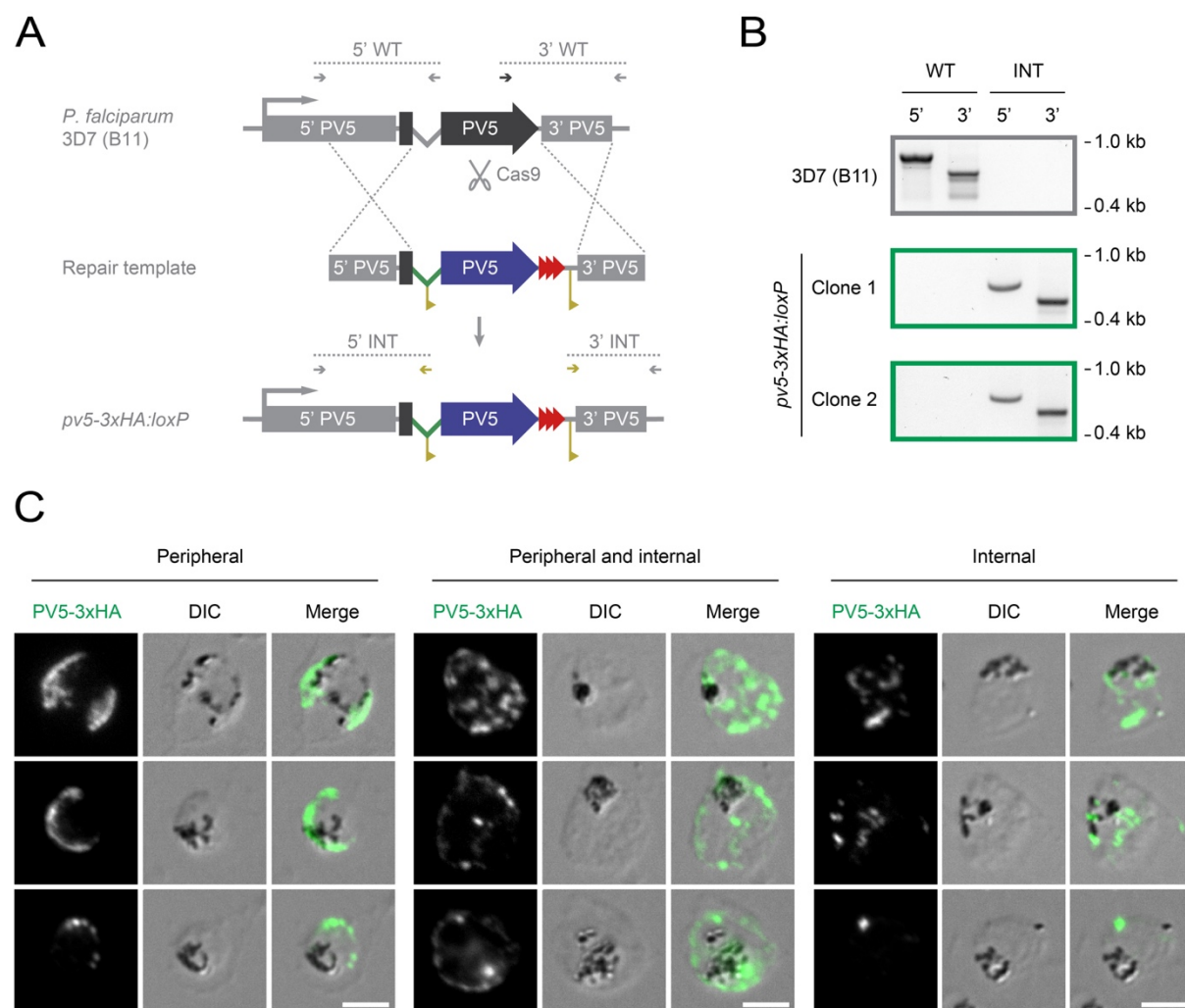


**Fig. S3.** PV5 localizes to the parasitophorous vacuole and to intraparasitic structures in *Plasmodium falciparum*.

(A) Genetic strategy for the generation of a conditional *PfPV5* knockout line. The endogenous *PfPV5* locus (dark grey) was targeted by Cas9-mediated double strand cleavage and repaired by homologous recombination with a synthetic template containing 5' and 3' homology arms (light grey), a 3xHA-tagged (red) re-codonised version of *PfPV5* (blue) and *loxP* sequences (yellow) within the artificial intron (green) and behind the *PfPV5* stop codon. Wild-type (WT) and integration-specific primer combinations (INT) are indicated by arrows and expected amplicons by dotted lines.

(B) Diagnostic PCR of the recipient *P. falciparum* 3D7 (B11) line (top) and of two isolated *pv5-3xHA:loxP* clones (bottom) using the primer combinations depicted in A.

(C) Dual localization of *PfPV5*. Immunofluorescence analysis was performed using anti-HA primary antibodies. Depicted are exemplary *pv5-3xHA:loxP* trophozoites and young schizonts demonstrating localization of *PfPV5* exclusively to the parasitophorous vacuole (PV,

891 left), to the PV and internal parasite structures (centre) or to intraparasitic structures only  
 892 (right). Shown are the signal of tagged *PfPV5* (left columns), differential interference contrast  
 893 images (centre columns) and a merge (right columns). Bars, 5  $\mu$ m.

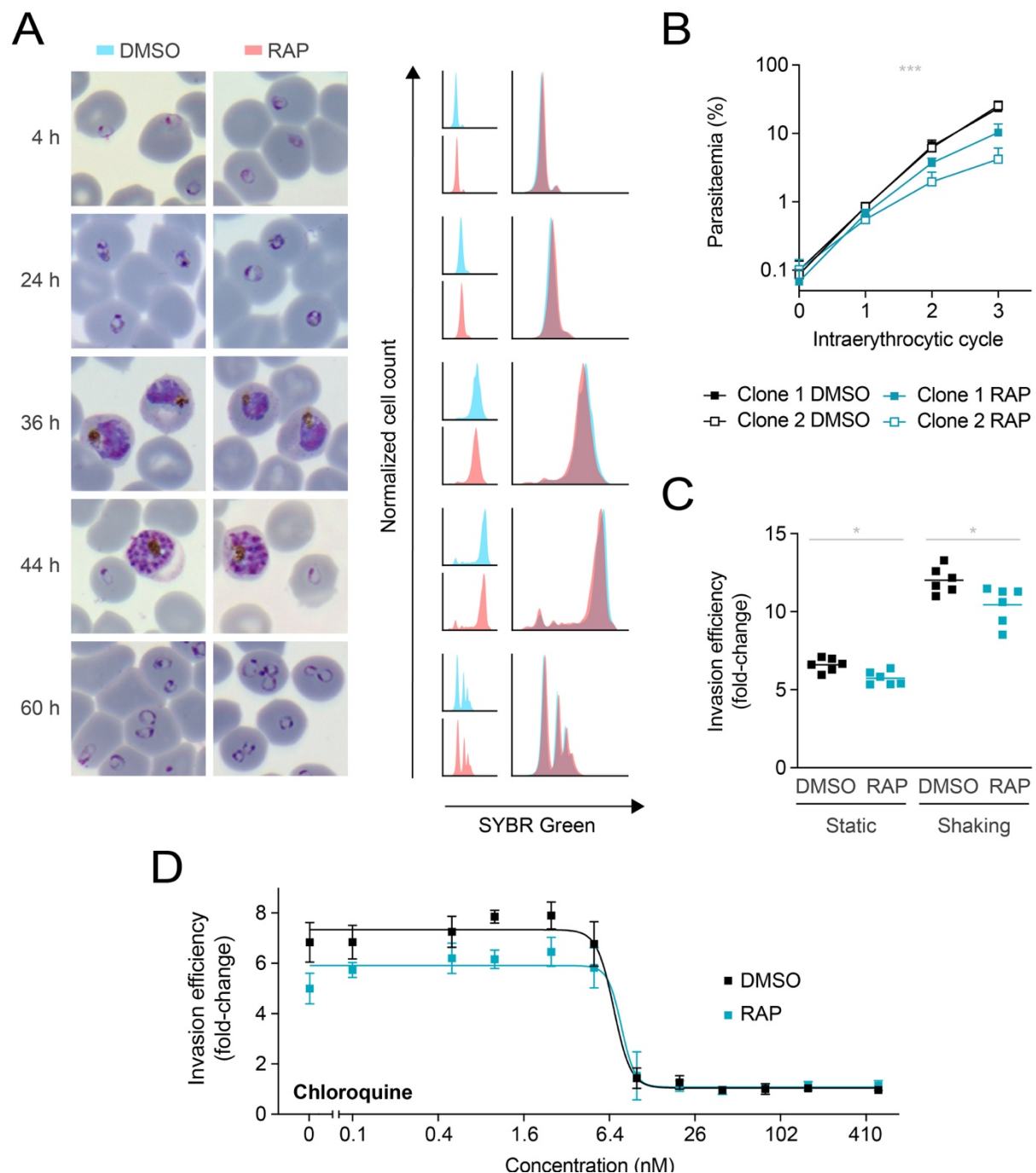


**Fig. S4.** Survival of *in vitro* cultivated *Plasmodium falciparum* in the absence of *PfPV5*.

(A) *PfPV5*-deficient parasites mature normally *in vitro*. Tightly synchronized *pv5::3xHA:loxP* ring stages were treated with dimethyl sulfoxide (DMSO, blue) or rapamycin (RAP, red) and then visualized by Giemsa staining 4, 24, 36, 44 and 60 hours later (left). In parallel, nuclear SYBR Green fluorescence was quantified by flow cytometry. Individual and merged histograms are depicted. Results are representative of two independent experiments.

(B) Asexual parasite proliferation is impaired upon loss of *PfPV5*. Shown are growth curves of two independent *pv5::3xHA:loxP* clonal lines upon treatment with DMSO or RAP,

respectively. Averaged parasite multiplication rates are 7.6 (DMSO) and 4.6 (RAP). Shown are mean values  $\pm$  SD. \*\*\*,  $P < 0.001$ ; Two-way ANOVA. N=6 independent infections.

(C) Impaired schizont to ring stage transition in the absence of *PfPV5*. Schizonts from DMSO- and RAP-treated *pv5::3xHA:loxP* cultures were added to fresh erythrocytes and incubated under static or shaking conditions for 24 hours. Shown is the fold-change in parasitaemia, depicted as individual and mean values (bars). \*,  $P < 0.05$ ; paired *t*-test. N=6 independent infections.

(D) *PfPV5*-deficient parasites retain normal sensitivity towards chloroquine. Shown is a dose-response analysis of DMSO- and RAP-treated *pv5::3xHA:loxP* parasites. Static ring stage cultures were treated with varying chloroquine concentrations and the transition into the following intraerythrocytic cycle was quantified. Depicted are mean values ( $\pm$  SD). N=3. Non-linear regression analysis yielded  $IC_{50}$  values of 6.9 nM (DMSO) and 7.8 nM (RAP).

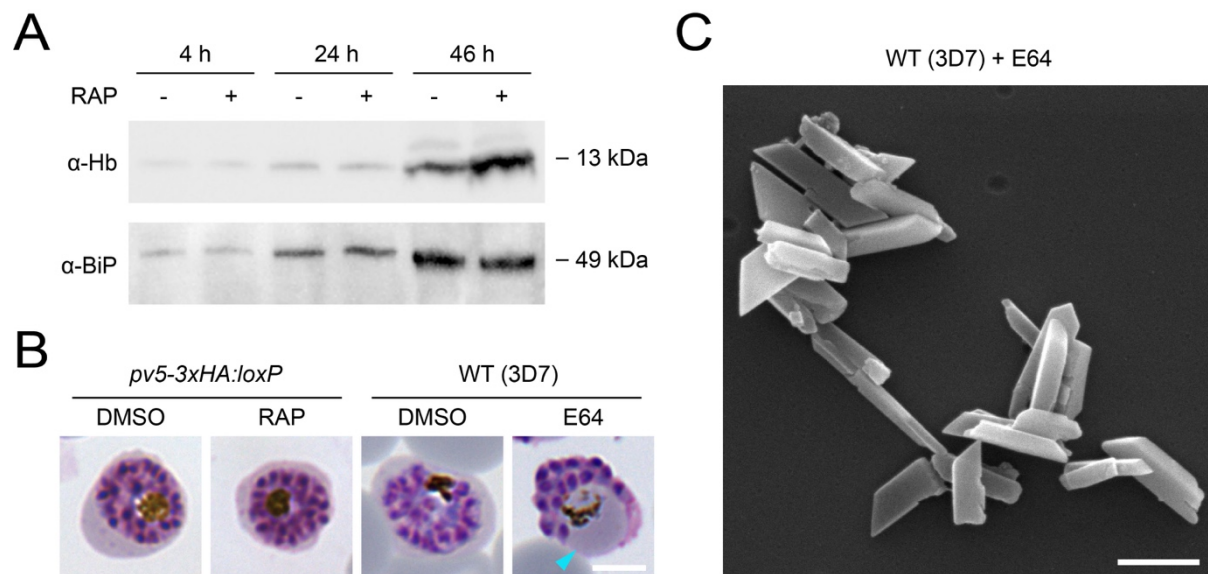


**Fig. S5.** Effective haemoglobin digestion in the absence of *PfPV5*.

(A) Western blot analysis of induced and non-induced *pv5-3xHA:loxP* parasites released from their host cells by saponin lysis at the indicated timepoints after invasion. Blots were probed with antibodies directed against human haemoglobin  $\alpha$  (Hb, top) and *PfBiP* (bottom). Densitometry suggests that RAP-treated *pv5-3xHA:loxP* parasites contain 104% (4 h), 93% (24 h) and 203% (46 h) of intact internalized haemoglobin  $\alpha$  in comparison to non-induced parasites.

(B) *PfPV5*-deficient schizonts exhibit no vacuolar bloating. Shown are *pv5-3xHA:loxP* parasites treated from the ring stage onward with dimethyl sulfoxide (DMSO) or rapamycin (RAP) and *Plasmodium falciparum* WT parasites treated from 24 hours post invasion onward with DMSO or E64. Cyan arrowhead, bloated food vacuole. Bar, 5  $\mu$ m.

(C) Inhibition of haemoglobin catabolism does not result in abnormal Hz morphology. Shown is a scanning electron micrograph of Hz crystals isolated from the E64-treated *P. falciparum* WT parasites shown in B. Bar, 500 nm.

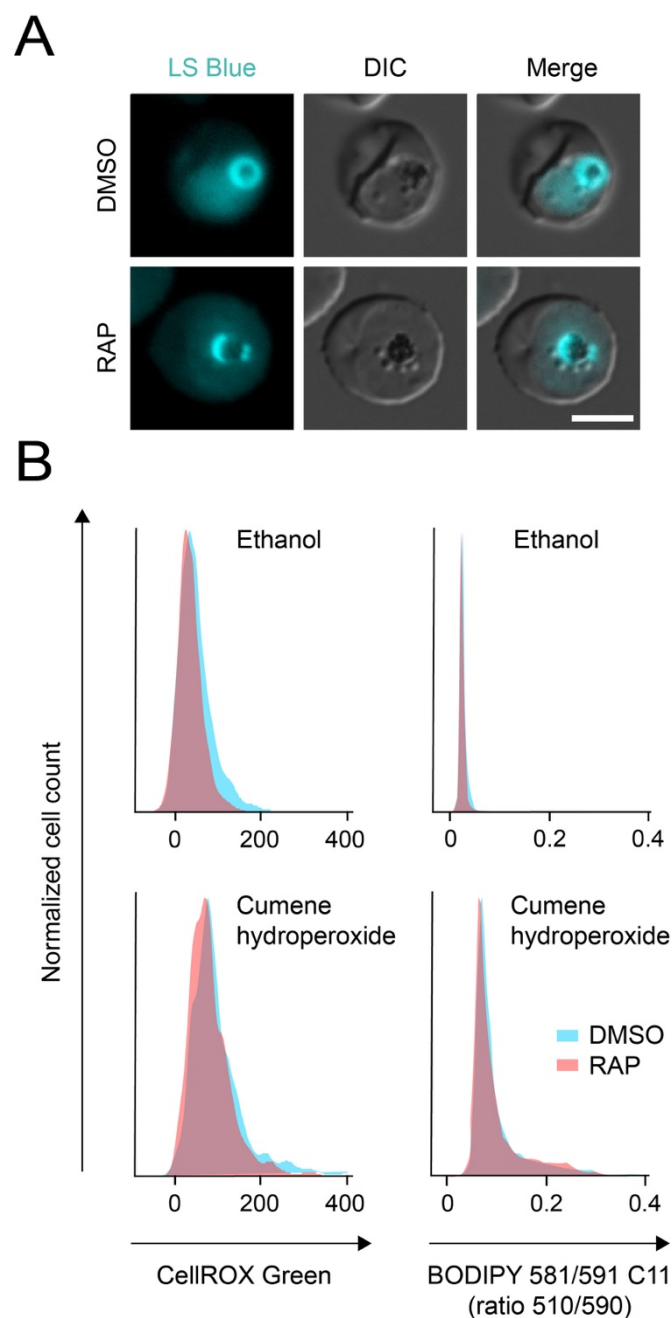


**Fig. S6.** Absence of *PfPV5* does not cause dissipation of the vacuolar pH gradient nor an increase in oxidative stress.

(A) *PfPV5*-deficient parasites maintain an intact and acidic food vacuole. Synchronized *pv5::3xHA:loxP* parasites were treated with dimethyl sulfoxide (DMSO) or rapamycin (RAP) from the ring stage onward and were stained with Lysosensor Blue DND-167 (LS Blue) 36 hours later. Shown are the LS Blue channel (cyan, left), differential interference contrast images (DIC, centre) and a merge (right). Bar, 5  $\mu$ m.

(B) No increased oxidative stress in the absence of *PfPV5*. Synchronized *pv5::3xHA:loxP* parasites were treated with DMSO or RAP from the ring stage onward, stained with the

940 oxidative stress sensor CellROX Green (left) or with the ratiometric lipid peroxidation dye  
 941 BODIPY 581/591 C11 (right) 36 hours later and analysed by flow cytometry. In addition,  
 942 parasites had been treated with the oxidative stress-inducing agent cumene hydroperoxide  
 943 (bottom) or with ethanol as the solvent control (top). Shown are the histograms of CellROX  
 944 Green fluorescence intensity or of the 510/590 nm fluorescence ratio of BODIPY 581/591 C11.  
 945 Results are representative of two independent experiments.  
 946

947 **Movie S1.** Absence of *Pf*PV5 ablates haemozoin movement within the food vacuole of  
 948 *Plasmodium falciparum*.  
 949 Shown are differential interference contrast recordings of dimethyl sulfoxide (DMSO, left) and  
 950 rapamycin-treated (RAP, right) *pv5::3xHA:loxP* parasites 36 hours following invasion. The  
 951 video contains 120 frames shown at a 4x acceleration. Elapsed time is indicated in the upper  
 952 right corner. Bar, 5  $\mu$ m.

953 **Table S1. Haemozoin crystal morphometry.**

	WT	<i>pv5-3xHA:loxP</i>		WT vs. DMSO	WT vs. RAP	DMSO vs. RAP
		DMSO	RAP			
Area ( $\mu\text{m}^2$ )	0.164 ( $\pm 0.088$ )	0.107 ( $\pm 0.052$ )	0.102 ( $\pm 0.039$ )	***	***	n.s.
Aspect ratio	3.673 ( $\pm 1.047$ )	2.781 ( $\pm 1.061$ )	1.604 ( $\pm 0.337$ )	***	***	***
Branching (%)	0	27.5	96.1			

954 n.s., non-significant; \*\*\*,  $P < 0.001$ ; One-way ANOVA and Tukey's multiple comparison test.  
955 N>300 crystals.

**Table S2. Primer sequences.**

Primer Name	Primer Sequence (restriction sites)	WT (bp) <sup>a</sup>	INT (bp) <sup>b</sup>	EX (bp) <sup>c</sup>	Use <sup>d</sup>	Target	Reference
NT-PbPV5-F- <i>Bam</i> HI	agttttgatccaaaatgaaattttatagcatttttgcaatg	707			TV	NT PbPV5	This study
NT-PbPV5-R- <i>Sac</i> II	agtattccgctgtttaataacatttctgattttttctcc				TV	NT PbPV5	This study
5'-PbPTEX88-F- <i>Bam</i> HI	aaatatgatccctttttgtgaaataaagtgtttgtg	1,496			TV	5' PbPTEX88	This study
5'-PbPTEX88-R- <i>Bam</i> HI	atatatgatcccaattttggggatttcaatcttttaag				TV	5' PbPTEX88	This study
5'-PbHSP101-F- <i>Bam</i> HI	ttaaaaggatccaaaattatacaatgcgtgtggc	1,489			TV	5' PbHSP101	This study
5'-PbHSP101-R- <i>Bam</i> HI	ttttcagatccattatagtaaatatagatataattttatcttcattc				TV	5' PbHSP101	This study
T7	taatacgactcactataggg				GT	T7	-
5'-PbPV5-F	gtgggtcgttattgtatttttaattattagg	1,440	1,206		GT	5' PbPV5	This study
CT-PbPV5-R1	gatggatcataaccagcaacg				GT	CT PbPV5	This study
5'-PbPTEX88-F	agtagcaagatataattgaaaagcc		1,091		GT	5' PbPTEX88	This study
5'-PbHSP101-F	tgcaactcattttattacgcc		1,177		GT	5' PbHSP101	This study
CT-PbPV5-F	taaaccogttgatgaaaacactactgttg	261			qPCR	CT PbPV5	This study
CT-PbPV5-R2	ggatcataaccagcaacgtaaaagagc				qPCR	CT PbPV5	This study
Pb18S-F	aagcattaaataaagcgaatacatccttac	134			qPCR	Pb18S-rRNA	(64)
Pb18S-R	ggagattggtttgacgtttatgtg				qPCR	Pb18S-rRNA	(64)
NT-PfPV5-F	attgattgttattatcattccag	24			gRNA	NT PfPV5	This study
NT-PfPV5-R1	aaacctggaaatgataataacaat				gRNA	NT PfPV5	This study
5'-PfPV5-F	aatgcggggaggaggagaaccc	836	730	2,006 / 1,260	GT	5' PfPV5	This study
NT-PfPV5-R2	acaactccatctatcaaaattaaag				GT	NT PfPV5	This study
CT-PfPV5-F	catgatcattatgtctaaatatagaacc	670			GT	CT PfPV5	This study
3'-PfPV5-R	atgtgaaaaaactacaaactatataccc		561	2,006 / 1,260	GT	3' PfPV5	This study
LoxP-F	taacttcgtatagcatacattatag				GT	loxP	This study
LoxP-R	aacttcgtataatgtatgctatag				GT	loxP	This study

<sup>a</sup> Sizes of Wild-type-specific PCR products.

<sup>b</sup> Sizes of integration-specific PCR products.

<sup>c</sup> Sizes of excision-diagnostic PCR products (non-excised / excised).

<sup>d</sup> Primers used for construction of Transfection Vectors (TV), for GenoTyping (GT), or quantitative real-time PCR - (qPCR). Used primer combinations are indicated in Figures 3A and *SI Appendix*, Figures S1A and S3A.